An Exploratory Investigation of a Slotted, Natural-Laminar-Flow Airfoil

Dan M. Somers
Airfoils, Incorporated, Port Matilda, Pennsylvania

NASA STI Program . . . in Profile

Since its founding, NASA has been dedicated to the advancement of aeronautics and space science. The NASA scientific and technical information (STI) program plays a key part in helping NASA maintain this important role.

The NASA STI program operates under the auspices of the Agency Chief Information Officer. It collects, organizes, provides for archiving, and disseminates NASA's STI. The NASA STI program provides access to the NASA Aeronautics and Space Database and its public interface, the NASA Technical Report Server, thus providing one of the largest collections of aeronautical and space science STI in the world. Results are published in both non-NASA channels and by NASA in the NASA STI Report Series, which includes the following report types:

- TECHNICAL PUBLICATION. Reports of completed research or a major significant phase of research that present the results of NASA programs and include extensive data or theoretical analysis. Includes compilations of significant scientific and technical data and information deemed to be of continuing reference value. NASA counterpart of peer-reviewed formal professional papers, but having less stringent limitations on manuscript length and extent of graphic presentations.

- TECHNICAL MEMORANDUM. Scientific and technical findings that are preliminary or of specialized interest, e.g., quick release reports, working papers, and bibliographies that contain minimal annotation. Does not contain extensive analysis.

- CONTRACTOR REPORT. Scientific and technical findings by NASA-sponsored contractors and grantees.

- CONFERENCE PUBLICATION. Collected papers from scientific and technical conferences, symposia, seminars, or other meetings sponsored or co-sponsored by NASA.

- SPECIAL PUBLICATION. Scientific, technical, or historical information from NASA programs, projects, and missions, often concerned with subjects having substantial public interest.

- TECHNICAL TRANSLATION. English-language translations of foreign scientific and technical material pertinent to NASA's mission.

Specialized services also include creating custom thesauri, building customized databases, and organizing and publishing research results.

For more information about the NASA STI program, see the following:

- Access the NASA STI program home page at *http://www.sti.nasa.gov*

- E-mail your question via the Internet to help@sti.nasa.gov

- Fax your question to the NASA STI Help Desk at 443-757-5803

- Phone the NASA STI Help Desk at 443-757-5802

- Write to:
  NASA STI Help Desk
  NASA Center for AeroSpace Information
  7115 Standard Drive
  Hanover, MD 21076-1320

NASA/CR–2012-217560

An Exploratory Investigation of a
Slotted, Natural-Laminar-Flow Airfoil

Dan M. Somers
Airfoils, Incorporated, Port Matilda, Pennsylvania

National Aeronautics and
Space Administration

Langley Research Center
Hampton, Virginia 23681-2199

April 2012

Acknowledgments

ABSTRACT

A 15-percent-thick, slotted, natural-laminar-flow (SNLF) airfoil, the S103, for general aviation applications has been designed and analyzed theoretically and verified experimentally in the Langley Low-Turbulence Pressure Tunnel. The two primary objectives of high maximum lift and low profile drag have been achieved. The constraints on the pitching moment and the airfoil thickness have been satisfied. The airfoil exhibits a rapid stall, which does not meet the design goal. Comparisons of the theoretical and experimental results show good agreement. Comparison with the baseline, NASA NLF(1)-0215F airfoil confirms the achievement of the objectives.

INTRODUCTION

The wing profile drag is the largest contributor to the total aircraft drag at cruise conditions for most aircraft. The wing profile drag contributes about one third of the total drag for transport aircraft. As the aircraft size decreases from transport through commuter to business jets and other general aviation (GA) aircraft and finally unmanned aerial vehicles (UAV's) and sailplanes, the percentage of the total aircraft drag due to the wing profile drag generally increases, primarily because the relative wing area increases, as shown in the following table.

Aircraft Type	Wing Profile Drag / Total Aircraft Drag
Transport	~ 1/3
Business jet	~ 1/3
Low-speed GA	> 1/3
UAV	1/3 to 1/2
Sailplane	> 1/2

To minimize wing profile drag, the figure of merit *FOM* applicable to aircraft having their wing area determined by a minimum-speed requirement (usually landing speed) should be maximized:

$$FOM = \frac{c_{l,max}}{c_{d,cruise}}$$

where $c_{l,max}$ is the section maximum lift coefficient and $c_{d,cruise}$ is the cruise section profile-drag coefficient. (See ref. 1.) Note that the figure of merit is expressed in terms of section (airfoil) characteristics, not aircraft characteristics. The figure of merit can be interpreted as follows. The wing area, and therefore the aircraft wetted area, can be reduced if a higher maximum lift coefficient is achieved, resulting in lower drag. The wing profile drag can also be reduced if a lower section profile-drag coefficient is achieved. This figure of merit applies to almost all classes of aircraft. For those aircraft having their wing area determined by a fuel-

volume requirement (e.g., business jets), reducing the section profile-drag coefficient is even more beneficial.

Three approaches have become accepted for the reduction of wing profile drag. One approach is to employ a high-lift system (e.g., leading-edge slat plus double- or triple-slotted, Fowler flap) to achieve a higher maximum lift coefficient. (See, for example, ref. 2.) This approach has several disadvantages. Almost no laminar flow can be achieved because of the disturbances introduced by the slat, which results in a high section profile-drag coefficient. The maximum lift coefficient is limited to about 4, which limits the reduction in wing area. High-lift systems are complex, both mechanically and structurally, resulting in higher weight and cost. This approach can provide a maximum wing profile-drag reduction of about 50 percent compared to a conventional, turbulent-flow wing with no high-lift system and has been adopted for all current transport aircraft. Active high-lift systems (e.g., blown flaps and circulation control) have demonstrated very high lift coefficients but the cost, complexity, and potentially disastrous failure modes have prevented their adoption for production aircraft.

A second approach is to employ a natural-laminar-flow (NLF) airfoil to achieve a lower profile-drag coefficient. (See, for example, ref. 3.) By appropriate airfoil shaping, extensive ($\geq$ 30-percent-chord) laminar flow can be achieved on both the upper and lower wing surfaces. The extent of laminar flow is limited to about 70-percent chord by the pressure-recovery gradient along the aft portion of the airfoil and by leading-edge sweep. The recovery gradient becomes steeper as the extent of the favorable gradient along the forward portion of the airfoil increases. The recovery gradient eventually reaches a limit beyond which trailing-edge separation occurs, resulting in a lower maximum lift coefficient and a correspondingly lower figure of merit. Leading-edge sweep restricts the extent of laminar flow because it introduces crossflow instabilities that lead to transition. This approach can also provide a wing profile-drag reduction of about 50 percent compared to a conventional, turbulent-flow wing and has been adopted for most current general aviation aircraft, including business jets, as well as unmanned aerial vehicles and all sailplanes. It does, however, require more stringent construction techniques.

A third approach is to employ a laminar-flow-control (LFC) airfoil to achieve a lower profile-drag coefficient. (See, for example, ref. 4.) By incorporating suction through porous or slotted, wing skins, 100-percent-chord laminar flow can be achieved on both the upper and lower wing surfaces. LFC systems are very complex, mechanically, structurally, and operationally, resulting in higher weight and cost. This approach can provide a wing profile-drag reduction of about 75 percent compared to a conventional, turbulent-flow wing but has yet to be adopted for any production aircraft.

For the present effort, a new approach, called a slotted, natural-laminar-flow (SNLF) airfoil, is employed. The SNLF airfoil concept is similar in nature to the slotted, supercritical airfoil concept (ref. 5).

<div align="center">SYMBOLS</div>

Values are given in both SI and U.S. Customary Units. Measurements and calculations were made in U.S. Customary Units.

C_p pressure coefficient, $\dfrac{p_l - p_\infty}{q_\infty}$

c airfoil chord, mm (in.)

c_c section chord-force coefficient, $\oint C_p \, d\left(\dfrac{z}{c}\right)$

c_d section profile-drag coefficient, $\displaystyle\int_{Wake} c_d' \, d\left(\dfrac{h}{c}\right)$

c_d' point drag coefficient (ref. 6)

c_l section lift coefficient, $c_n \cos\alpha - c_c \sin\alpha$

c_m section pitching-moment coefficient about quarter-chord point,

$$-\oint C_p \left(\dfrac{x}{c} - 0.25\right) d\left(\dfrac{x}{c}\right) + \oint C_p \left(\dfrac{z}{c}\right) d\left(\dfrac{z}{c}\right)$$

c_n section normal-force coefficient, $-\oint C_p \, d\left(\dfrac{x}{c}\right)$

h vertical height in wake profile, mm (in.)

M free-stream Mach number

p static pressure, Pa (lbf/ft^2)

q dynamic pressure, Pa (lbf/ft^2)

R Reynolds number based on free-stream conditions and airfoil chord

t airfoil thickness, mm (in.)

x airfoil abscissa, mm (in.)

y model span station, $y = 0$ at midspan, mm (in.)

z airfoil ordinate, mm (in.)

α angle of attack relative to x-axis, deg

Δx change in chordwise position of aft element, mm (in.)

Δz change in vertical position of aft element, mm (in.)

$\Delta\theta$	change in angle of aft element, deg

δ_f	flap deflection, positive downward, deg

Subscripts:

l	local point on airfoil
ll	lower limit of low-drag range
max	maximum
ul	upper limit of low-drag range
0	zero lift
∞	free-stream conditions

Abbreviations:

LFC	laminar flow control
ls	lower surface
NLF	natural laminar flow
SNLF	slotted, natural laminar flow
us	upper surface

AIRFOIL DESIGN

OBJECTIVES AND CONSTRAINTS

The design specifications for the airfoil are contained in table I. The specifications are essentially identical to those for the baseline airfoil, the NASA NLF(1)-0215F (ref. 7), except for the constraint on the zero-lift pitching-moment coefficient, which is more negative.

Two primary objectives are evident. The first objective is to achieve a maximum lift coefficient of at least 1.72 for a Reynolds number of 3×10^6. A requirement related to this objective is that the maximum lift coefficient not decrease significantly with transition fixed near the leading edge on both surfaces. In addition, the airfoil should exhibit docile stall characteristics. The second objective is to obtain low profile-drag coefficients from a cruise lift coefficient of 0.20 for a Reynolds number of 9×10^6 to a climb lift coefficient of 1.00 for a

Reynolds number of 6×10^6. Because this is a low-speed application, the flow is considered incompressible (i.e., $M = 0$).

Two major constraints were placed on the design of the airfoil. First, the zero-lift pitching-moment coefficient must be no more negative than –0.20. Second, the airfoil thickness must equal 15-percent chord.

PHILOSOPHY

Given the above objectives and constraints, certain characteristics of the design are apparent. The following sketch illustrates a drag polar that meets the goals for this design.
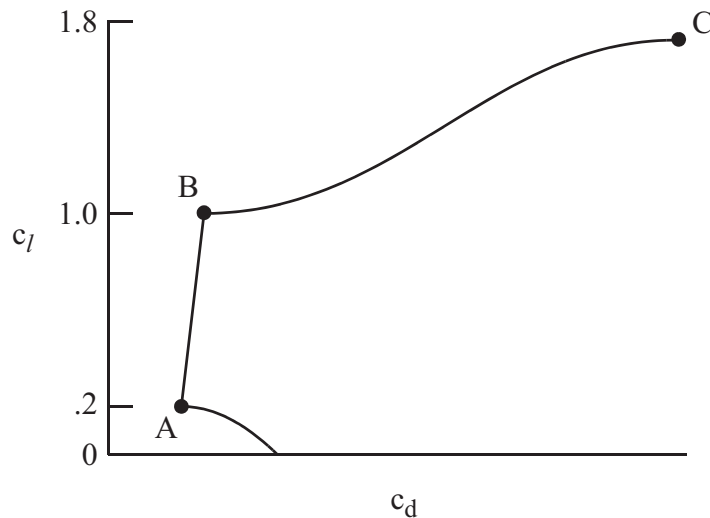
Sketch 1

Point A is the lower limit of the low-drag, lift-coefficient range; point B, the upper limit. The profile-drag coefficient increases very rapidly outside the low-drag range because boundary-layer transition moves quickly toward the leading edge with increasing (or decreasing) lift coefficient. This feature results in a leading edge that produces a suction peak at higher lift coefficients, which ensures that transition on the upper surface will occur very near the leading edge. Thus, the maximum lift coefficient, point C, occurs with turbulent flow along the entire upper surface and, therefore, should be relatively insensitive to roughness at the leading edge.

A two-element airfoil concept is used to meet the design requirements. The pressure distribution at point A is illustrated in sketch 2.

C_p

-4.0 MSES v 3.0

-3.5

-3.0

-2.5

-2.0

-1.5

-1.0

-0.5

0.0

0.5

1.0

S103
Mach = 0.100
Re   = 9.000×10^6
Alfa = -2.250
CL   = 0.1998
CD   = 0.00288
CM   = -0.1675
L/D = 69.50
Ncrit = 9.00

us
ls
us
ls
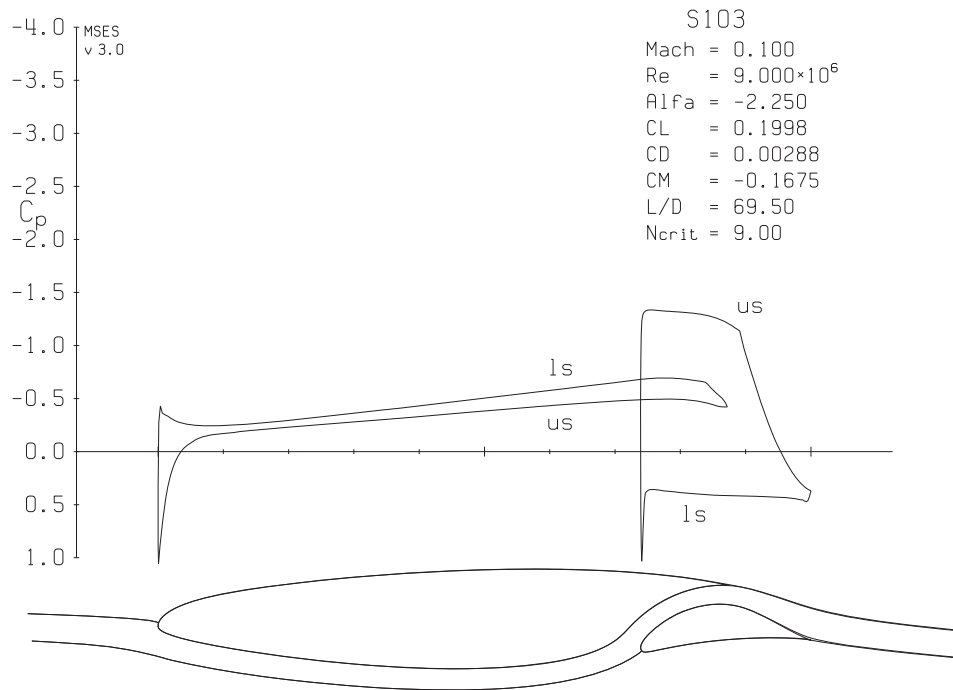
Sketch 2

Because the aft element eliminates the requirement that the pressure at the trailing edge of the fore element recover to free stream (see ref. 8), the favorable pressure gradient can extend further aft. For the slotted, natural-laminar-flow (SNLF) airfoil concept, the favorable gradient extends along both surfaces of the fore element to near its trailing edge. Thus, the fore element is almost entirely laminar. The aft element then provides the necessary recovery to free-stream pressure. Because the wake of the fore element does not impinge on the aft element, the aft element can also achieve significant extents of laminar flow.

The SNLF airfoil concept allows the extent of natural laminar flow to be increased beyond the limit previously discussed. Thus, the concept allows lower profile-drag coefficients to be achieved without having to resort to the complexity and cost of LFC. The concept also allows high maximum lift coefficients to be achieved without variable geometry. The SNLF airfoil shape is not radically different from conventional airfoil shapes—no more than conventional, NLF airfoils are from conventional, turbulent-flow airfoils. Unlike conventional airfoils with slotted flaps, however, the SNLF airfoil has no nested configuration; the slot between the fore and aft elements is always open.

EXECUTION

The Eppler Airfoil Design and Analysis Code (refs. 9 and 10), a single-element code, was used to design the initial fore- and aft-element shapes. The MSES code (ref. 11), a multi-element code, was used to refine the shapes in the two-element configuration.

The airfoil is designated the S103. The airfoil shape is shown in figure 1. The airfoil thickness is 15-percent chord, which satisfies the design constraint.

EXPERIMENTAL PROCEDURE

WIND TUNNEL

The Langley Low-Turbulence Pressure Tunnel (refs. 12 and 13) is a closed-throat, single-return tunnel (fig. 2) that can be operated at stagnation pressures from 100 to 1000 kPa (1 to 10 atm). The unit Reynolds number can be varied from 1×10^6 to 49×10^6 per meter $(0.3 \times 10^6$ to 15×10^6 per foot); the Mach number can be varied from 0.05 to 0.47. The turbulence level in the test section is generally below 0.05 percent for unit Reynolds numbers up to 13×10^6 per meter $(4 \times 10^6$ per foot) at Mach numbers up to 0.15 (ref. 14).

The test section is 914.4 mm (36.00 in.) wide by 2286 mm (90.00 in.) high. Hydraulically actuated circular plates provide positioning and attachment for the two-dimensional model (fig. 3). The plates, about 86 cm (34 in.) in diameter, are flush with the tunnel side-walls and rotate with the model. The axis of rotation coincided approximately with the mid-chord of the model, which was mounted horizontally between the plates. The gaps between the model and the plates were sealed.

MODEL

The aluminum, wind-tunnel model was fabricated by Advanced Technologies, Incorporated, Newport News, Virginia, using a numerically controlled milling machine. The model had a chord of 762.00 mm (30.000 in.) and a span of 914.4 mm (36.00 in.). Upper- and lower-surface orifices were located to one side of midspan at the staggered positions listed in table II. In addition, an abbreviated, chordwise row of orifices was located near each tunnel sidewall to monitor the two-dimensionality of the flow. All the orifices were 0.51 mm (0.020 in.) in diameter with their axes perpendicular to the surface. The surface of the model had been polished to ensure an aerodynamically smooth finish. The measured model contour was within 0.1 mm (0.004 in.) of the prescribed shape.

The aft element was mounted directly to the circular plates, not to the fore element. The mounting system allowed the aft-element chordwise position, vertical position, and angle to be varied independently. For several test runs, the aft element was fitted with trailing-edge pieces that simulated 0°, 5°, and 10° deflections of a sealed, lower-surface-hinged, simple flap. The location of the flap-hinge point was $x/c = 0.9610$, $z/c = -0.0184$. Thus, the flap

had a chord of approximately 15 percent of the aft-element chord. (See fig. 1.) No orifices were located in the trailing-edge pieces.

WAKE RAKE

A traversing, wake rake was mounted from the tunnel strut (fig. 3). The wake rake employed 25 total-pressure tubes, 13 mm (0.50 in.) apart, and 2 static-pressure tubes. The rake was positioned spanwise at the tunnel centerline (i.e., at the model midspan). The tips of the total-pressure tubes were located 0.93-chord downstream of the trailing edge of the model. A traverse mechanism incrementally positioned the rake vertically.

INSTRUMENTATION

Measurements of the pressures on the model and in the wake were made by an electronically scanned, pressure-transducer system. Basic tunnel pressures were measured with precision quartz manometers. Data were obtained and recorded by an electronic data-acquisition system.

METHODS

The pressures measured on the model were reduced to standard pressure coefficients and numerically integrated to obtain section normal- and chord-force coefficients and section pitching-moment coefficients about the quarter-chord point. To obtain more precise coefficients for the test runs involving the aft-element flap, the measured pressure distributions were extrapolated to simulate the pressures eliminated by the model modification. Section profile-drag coefficients were computed from the wake total and static pressures by the method of reference 6.

Standard, low-speed, wind-tunnel boundary corrections (ref. 15) have been applied to the section characteristics. The wake-rake total-pressure-tube displacement correction (ref. 6) has been taken into account.

TESTS

The model was tested at Reynolds numbers based on airfoil chord of 3×10^6, 6×10^6, and 9×10^6 and a Mach number of 0.1 with transition free. No transition-fixed measurements were made.

The aft element was rotated $-1.0°$ (nose down) about $x/c = 0.8321$, $z/c = 0.0002$ and translated $-0.0017c$ chordwise (forward) and $-0.0017c$ vertically (downward) from the design position for all the results presented except those for a Reynolds number of 9×10^6. For these

results, the aft element was rotated and translated chordwise the same amounts but not translated vertically.

DISCUSSION OF RESULTS

EXPERIMENTAL RESULTS

Pressure Distributions

The pressure distributions at various angles of attack for a Reynolds number of 3.0×10^6 and a Mach number of 0.10 with transition free are shown in figure 4. At an angle of attack of –4.15° (fig. 4(a)), a leading-edge pressure peak exists on the lower surface of the fore element whereas a favorable pressure gradient exists along the upper surface almost to the trailing edge of the fore element. An essentially flat gradient exists along the forward half of the upper surface of the aft element whereas an adverse gradient exists along almost all the lower surface of the aft element. A short laminar separation bubble, typical of the low Reynolds number of the aft element (0.8×10^6), is discernible on the upper surface around 60 percent of the aft-element chord. As the angle of attack is increased, the pressure peak on the lower surface of the fore element decreases in magnitude. At an angle of attack of –2.10° (fig. 4(c)), which corresponds roughly to the lower limit of the low-drag, lift-coefficient range, the peak no longer causes transition near the leading edge. At an angle of attack of –1.07° (fig. 4(d)), a favorable gradient exists along the lower surface of the fore element to about 65-percent chord. As the angle of attack in increased further, the pressure gradient along the forward portion of the upper surface of the fore element becomes less favorable until, at an angle of attack of –0.05° (fig. 4(e)), it is slightly adverse. At an angle of attack of 0.97° (fig. 4(f)), which corresponds to the upper limit of the low-drag range, the gradient along the forward portion of the upper surface of the fore element is still insufficiently adverse to cause transition to move forward. As the angle of attack is increased even further, the pressure peak near the leading edge on the upper surface of the fore element becomes sharper and moves forward (figs. 4(g)–4(l)) until, at an angle of attack of 8.12° (fig. 4(m)), it reaches the leading edge. As the angle of attack is increased still further, the leading-edge peak increases in magnitude (figs. 4(n)–4(t)). The maximum lift coefficient occurs just beyond an angle of attack of 16.29° (fig. 4(u)). At an angle of attack of 17.27° (fig. 4(v)), the leading-edge peak decreases slightly in magnitude and then collapses at an angle of attack of 18.04° (fig. 4(w)), indicating that almost the entire upper surface of the fore element is separated. The upper surface of the aft element remains attached, however. The pressure distribution on the aft element changes little with angle of attack, except for post stall (fig. 4(w)), because the incoming flow angle for the aft element is fixed by the fore element.

The pressure distributions for a Reynolds number of 6.1×10^6 and a Mach number of 0.10 (not shown) are nearly identical to those for a Reynolds number of 3.0×10^6 and a Mach number of 0.10 (fig. 4). Those for a Reynolds number of 9.1×10^6 and a Mach number of 0.10 are significantly different, however, as illustrated in figure 5. The pressure distribution along the upper surface of the aft element probably includes three-dimensional effects, a conclusion supported by the pressure distributions near the tunnel sidewalls. The three dimen-

sionality possibly results from premature transition on the upper surface of the aft element caused by the orifices or the sidewalls.

The effect of aft-element flap deflection on the pressure distribution is illustrated in figure 6. The increased circulation on the aft element due to the positive flap deflection induces higher velocities and, therefore, lower pressures on the lower surface of the fore element in the slot.

Section Characteristics

Reynolds number effects.- The section characteristics at a Mach number of 0.10 with transition free are shown in figure 7. For a Reynolds number of 3.0×10^6 (fig. 7(a)), the maximum lift coefficient is 2.00, which meets the design objective of $c_{l,\max} \geq 1.72$. The airfoil exhibits a rapid stall, which does not meet the design goal of docile stall characteristics. For a Reynolds number of 6.1×10^6 (fig. 7(b)), low profile-drag coefficients are predicted over the range of lift coefficients from 0.16 to 0.39. Thus, the upper limit of the low-drag range is below the design objective of $c_{l,\mathrm{ul}} = 1.00$, primarily to meet other, more important goals. The zero-lift pitching-moment coefficient is –0.14, which satisfies the design constraint of $c_{m,0} \geq -0.20$.

The effect of Reynolds number on the section characteristics at a Mach number of 0.10 with transition free is summarized in figure 8. In general, the zero-lift angle of attack, the lift-curve slope, and the pitching-moment coefficient are relatively unaffected by Reynolds number. The maximum lift coefficient increases with increasing Reynolds number whereas the minimum drag coefficient and the width of the low-drag range decrease.

Effect of aft-element position.- The drag coefficients within the low-drag range are essentially unaffected by variations in the aft-element position and angle over the following ranges: $-0.0033c \leq \Delta x \leq 0.0017c$, $-0.0033c \leq \Delta z \leq 0$, and $-1° \leq \Delta\theta \leq 0°$.

Effect of aft-element flap deflection.- The effect of aft-element flap deflection on the section characteristics is shown in figure 9. The low-drag range is shifted to higher lift coefficients with increasing flap deflection. (See ref. 4.)

COMPARISON OF THEORETICAL AND EXPERIMENTAL RESULTS

The theoretical results were computed using the method of reference 11. The computations were performed with transition free using a critical amplification factor of 9. Note that the method of reference 11 does not model the effect of Görtler instabilities (ref. 16) on transition. A cursory evaluation of this effect indicates that these instabilities may lead to transition in the concave region of the lower surface of the fore element.

Pressure Distributions

The comparison of the theoretical and experimental pressure distributions for a Reynolds number of 3.0×10^6 and a Mach number of 0.10 with transition free is shown in figure 10. At an angle of attack of $-3.12°$ (fig. 10(a)), which is below the low-drag range, the magnitudes of the pressure coefficients are overpredicted but the pressure gradients are predicted well, particularly on the fore element. The circulation is predicted well on the fore element but overpredicted on the aft element, which probably causes the overprediction of the magnitudes of the pressure coefficients on the lower surface of the fore element in the slot. The method of reference 11 also predicts the laminar separation bubble on the upper surface of the aft element. At an angle of attack of $-1.07°$ (fig. 10(b)), which is within the low-drag range, the agreement between the predicted and measured pressure distributions is better, particularly on the aft element. At an angle of 6.07° (fig. 10(c)), which is above the low-drag range, and at an angle of attack of 16.29° (fig. 10(d)), which is just below that for the maximum lift coefficient, the magnitudes of the pressure coefficients are overpredicted but the pressure gradients are predicted well. Overall, the agreement between the theoretical and experimental pressure distributions is good.

Section Characteristics

The comparisons of the theoretical and experimental section characteristics for Reynolds numbers of 3.0×10^6 and 6.1×10^6 at a Mach number of 0.10 with transition free are shown in figure 11. In general, the lift-curve slope, the maximum lift coefficient, the width of the low-drag range, and the magnitude of the pitching-moment coefficient are overpredicted. The drag coefficient is underpredicted. Overall, however, the agreement between the theoretical and experimental section characteristics is good for a two-element airfoil.

COMPARISON WITH BASELINE, NASA NLF(1)-0215F AIRFOIL

The comparison of the experimental section characteristics of the S103 and baseline, NASA NLF(1)-0215F (ref. 7) airfoils at a Mach number of 0.1 with transition free is shown in figure 12. Note that the NLF(1)-0215F airfoil incorporates a 25-percent-chord, simple flap. For a Reynolds number of 3×10^6 (fig. 12(a)), the S103 airfoil exhibits higher drag coefficients for lift coefficients lower than about 1.5 and lower drag coefficients for higher lift coefficients, less negative pitching-moment coefficients for angles of attack lower than about 11° and more negative pitching-moment coefficients for higher angles of attack, and a more rapid stall than does the NLF(1)-0215F airfoil with a flap deflection of 10°. The maximum lift coefficient of the S103 airfoil is 12 percent higher than that of the NLF(1)-0215F airfoil with a flap deflection of 10°. For a Reynolds number of 6×10^6 (fig. 12(b)), the S103 airfoil exhibits slightly lower drag coefficients within the low-drag range, a narrower low-drag range, and more negative pitching-moment coefficients than does the NLF(1)-0215F airfoil with a flap deflection of $-10°$. The minimum drag coefficient of the S103 airfoil is 7 percent lower than that of the NLF(1)-0215F airfoil with a flap deflection of $-10°$.

CONCLUDING REMARKS

A 15-percent-thick, slotted, natural-laminar-flow (SNLF) airfoil, the S103, for general aviation applications has been designed and analyzed theoretically and verified experimentally in the Langley Low-Turbulence Pressure Tunnel. The two primary objectives of high maximum lift coefficient and low profile-drag coefficients have been achieved. The constraints on the pitching-moment coefficient and the airfoil thickness have been satisfied. The airfoil exhibits a rapid stall, which does not meet the design goal. Comparisons of the theoretical and experimental results show good agreement. Comparison with the baseline, NASA NLF(1)-0215F airfoil confirms the achievement of the objectives.

REFERENCES

1. Maughmer, Mark D.; and Somers, Dan M.: Figures of Merit for Airfoil/Aircraft Design Integration. AIAA Paper 88-4416, Sept. 1988.

2. Smith, A. M. O.: High-Lift Aerodynamics. AIAA Paper 74-939, Aug. 1974.

3. Jacobs, Eastman N.: Preliminary Report on Laminar-Flow Airfoils and New Methods Adopted for Airfoil and Boundary-Layer Investigations. NACA WR L-345, 1939 (formerly, NACA ACR).

4. Pfenninger, Werner: Investigations on Reductions of Friction on Wings, in Particular by Means of Boundary Layer Suction. NACA TM 1181, 1947. (Translated from Mitteilungen aus dem Institut für Aerodynamik an der Eidgenössischen Technischen Hochschule Zürich, Nr. 13, 1946.)

5. Whitcomb, Richard T.; and Clark, Larry R.: An Airfoil Shape for Efficient Flight at Supercritical Mach Numbers. NASA TM X-1109, 1965.

6. Pankhurst, R. C.; and Holder, D. W.: Wind-Tunnel Technique. Sir Isaac Pitman & Sons, Ltd. (London), 1965.

7. Somers, Dan M.: Design and Experimental Results for a Flapped Natural-Laminar-Flow Airfoil for General Aviation Applications. NASA TP-1865, 1981.

8. Maughmer, Mark D.: Trailing Edge Flow Conditions as a Factor in Airfoil Design. Ph.D. Dissertation, Univ. of Illinois, 1983.

9. Eppler, Richard: Airfoil Design and Data. Springer-Verlag (Berlin), 1990.

10. Eppler, Richard: Airfoil Program System "PROFIL00." User's Guide. Richard Eppler, c.2001.

11. Drela, M.: Design and Optimization Method for Multi-Element Airfoils. AIAA Paper 93-0969, Feb. 1993.

12. Von Doenhoff, Albert E.; and Abbott, Frank T., Jr.: The Langley Two-Dimensional Low-Turbulence Pressure Tunnel. NACA TN 1283, 1947.

13. McGhee, Robert J.; Beasley, William D.; and Foster, Jean M.: Recent Modifications and Calibration of the Langley Low-Turbulence Pressure Tunnel. NASA TP-2328, 1984.

14. Wlezien, R. W.; Spencer, S. A.; and Grubb, J. P.: Comparison of Flow Quality in Subsonic Pressure Tunnels. AIAA Paper 94-2503, June 1994.

15. Allen, H. Julian; and Vincenti, Walter G.: Wall Interference in a Two-Dimensional-Flow Wind Tunnel, With Consideration of the Effect of Compressibility. NACA Rep. 782, 1944. (Supersedes NACA WR A-63.)

16. Görtler, H.: On the Three-Dimensional Instability of Laminar Boundary Layers on Concave Walls. NACA TM 1375, 1954.

TABLE I.- AIRFOIL DESIGN SPECIFICATIONS

Parameter	Value	Reynolds number R	Mach number M
Maximum lift coefficient $c_{l,max}$	≥ 1.72	3×10^6	
Lower limit of low-drag, lift-coefficient range $c_{l,ll}$	0.20	9×10^6	
Upper limit of low-drag, lift-coefficient range $c_{l,ul}$	1.00	6×10^6	0
Zero-lift pitching-moment coefficient $c_{m,0}$	≥ -0.20	9×10^6	
Thickness t/c	0.15		

TABLE II.- MODEL ORIFICE LOCATIONS

[c = 762.00 mm (30.000 in.)]

(a) Fore element

Upper surface		Lower surface	
x/c	y, mm (in.)	x/c	y, mm (in.)
–0.00007	284.6 (11.205)	0.00160	281.0 (11.062)
.00117	288.2 (11.345)	.00537	279.8 (11.015)
.00530	287.5 (11.317)	.01277	278.9 (10.982)
.01210	286.4 (11.277)	.02160	277.4 (10.923)
.02133	285.0 (11.221)	.03307	275.8 (10.860)
.03307	283.0 (11.143)	.04747	273.8 (10.778)
.04690	280.9 (11.060)	.06410	271.4 (10.686)
.06440	278.8 (10.976)	.08317	268.6 (10.576)
.08293	275.9 (10.863)	.10433	265.6 (10.458)
.10440	272.8 (10.742)	.12730	262.3 (10.325)
.12760	269.7 (10.617)	.15253	258.5 (10.178)
.15287	266.1 (10.478)	.18010	254.6 (10.024)
.17967	262.2 (10.323)	.20820	251.0 (9.880)
.20813	258.4 (10.173)	.23820	247.0 (9.723)
.23810	254.1 (10.003)	.26920	242.3 (9.541)
.26890	249.7 (9.831)	.30130	238.3 (9.382)
.30110	245.4 (9.663)	.33413	233.6 (9.197)
.33460	240.7 (9.478)	.36780	229.0 (9.015)
.36767	236.4 (9.307)	.40200	224.5 (8.837)
.40180	231.8 (9.126)	.43633	219.6 (8.646)
.43607	227.1 (8.940)	.46987	214.9 (8.462)
.47030	222.4 (8.756)	.50403	210.2 (8.276)
.50427	217.8 (8.576)	.53743	205.7 (8.100)
.53787	213.3 (8.396)	.57030	201.3 (7.924)
.57067	208.6 (8.213)	.60297	197.0 (7.755)
.60277	204.3 (8.043)	.63343	192.4 (7.573)
.63373	199.9 (7.871)	.64890	190.5 (7.499)
.66373	195.8 (7.710)	.66357	188.1 (7.407)
.69227	191.7 (7.547)	.67793	186.2 (7.331)
.71880	188.3 (7.412)	.69237	184.3 (7.255)
.74420	184.6 (7.269)	.70627	182.0 (7.167)
.76697	181.2 (7.135)	.71867	180.2 (7.095)
.78843	178.3 (7.019)	.73120	178.5 (7.026)
.80773	175.5 (6.908)	.74400	176.5 (6.948)
.82403	173.0 (6.811)	.75557	175.0 (6.889)
.83857	171.0 (6.732)	.76683	173.5 (6.830)
.85063	169.2 (6.660)	.77820	171.7 (6.758)
.85993	167.9 (6.612)	.78877	170.0 (6.691)
.86653	166.9 (6.570)	.80767	167.2 (6.583)
.87070	165.8 (6.527)	.82410	164.7 (6.485)
.87177	163.7 (6.443)	.83797	163.1 (6.423)
		.85030	161.2 (6.346)
		.85937	159.8 (6.291)
		.86643	158.8 (6.253)
		.87060	157.7 (6.210)

TABLE II.- Concluded

[c = 762.00 mm (30.000 in.)]

(b) Aft element

Upper surface		Lower surface	
x/c	y, mm (in.)	x/c	y, mm (in.)
0.74010	105.2 (4.142)	0.73910	106.2 (4.181)
.74393	103.8 (4.088)	.74220	112.6 (4.434)
.74940	102.8 (4.048)	.74893	111.7 (4.398)
.75683	101.7 (4.003)	.76093	110.0 (4.332)
.76597	100.2 (3.945)	.77743	107.5 (4.233)
.77720	98.8 (3.890)	.79720	104.9 (4.128)
.79007	97.0 (3.818)	.81970	101.7 (4.003)
.80447	95.0 (3.741)	.84423	98.4 (3.875)
.81990	92.7 (3.651)	.86960	94.9 (3.735)
.83567	90.3 (3.557)	.89503	91.3 (3.593)
.85270	88.2 (3.471)	.91947	88.0 (3.466)
.86967	85.7 (3.373)	.94197	85.0 (3.348)
.88630	83.2 (3.275)	.96207	82.2 (3.237)
.90293	80.9 (3.187)	.97833	79.9 (3.146)
.91890	78.5 (3.091)	.99010	78.1 (3.076)
.93397	76.1 (2.995)	.99750	77.1 (3.037)
.94873	79.6 (3.133)		
.96127	82.3 (3.242)		
.97253	85.2 (3.354)		
.98200	87.1 (3.431)		
.98983	89.0 (3.503)		
.99530	90.3 (3.556)		
.99843	91.0 (3.584)		
1.00010	84.3 (3.320)		
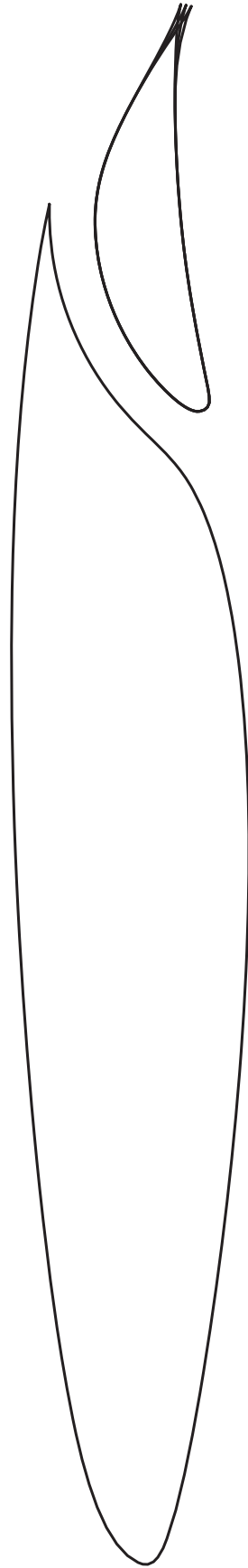
Figure 1.- S103 airfoil shape.

Low-Turbulence Pressure Tunnel
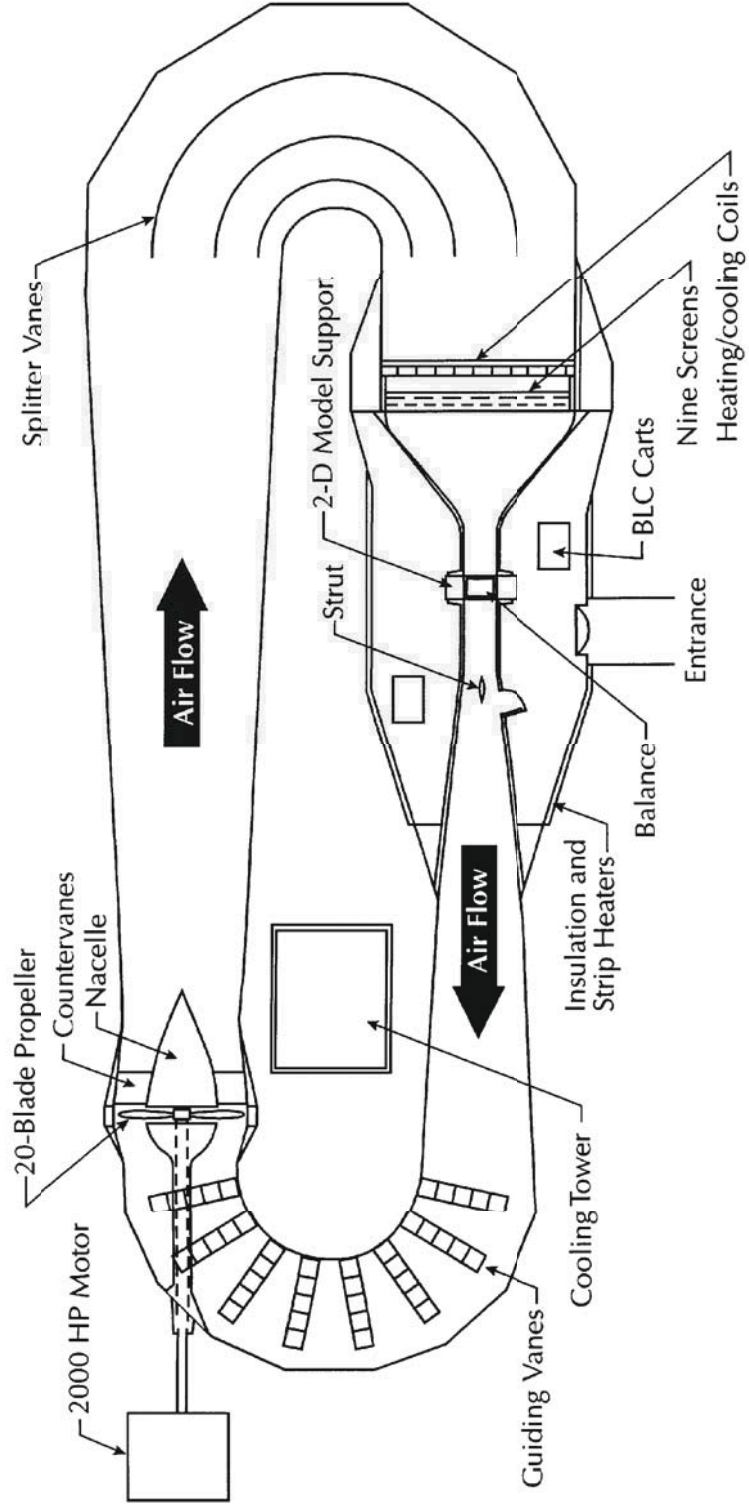
Figure 2.- Langley Low-Turbulence Pressure Tunnel.
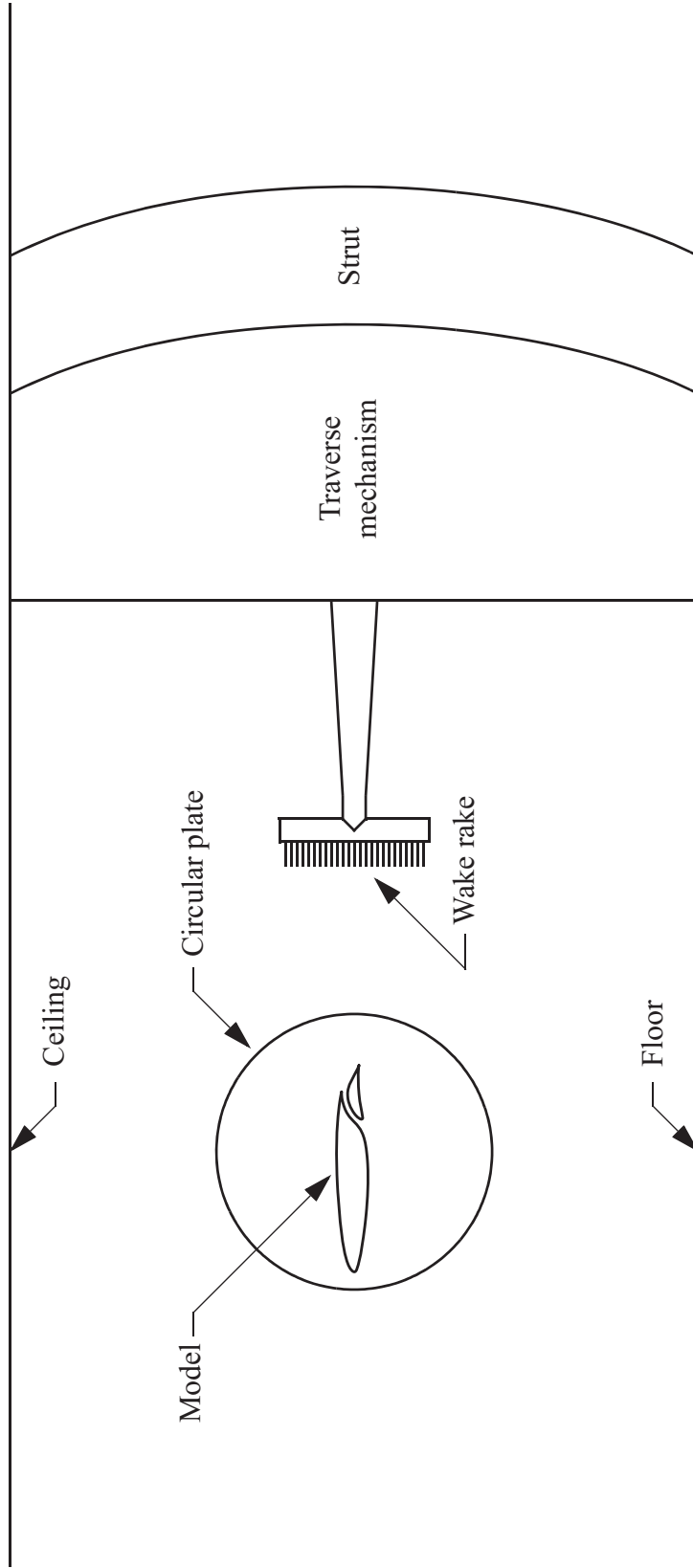
Figure 3.- Sketch of model and wake rake mounted in test section.

Ceiling

Circular plate

Model

Wake rake

Strut

Traverse mechanism

Floor
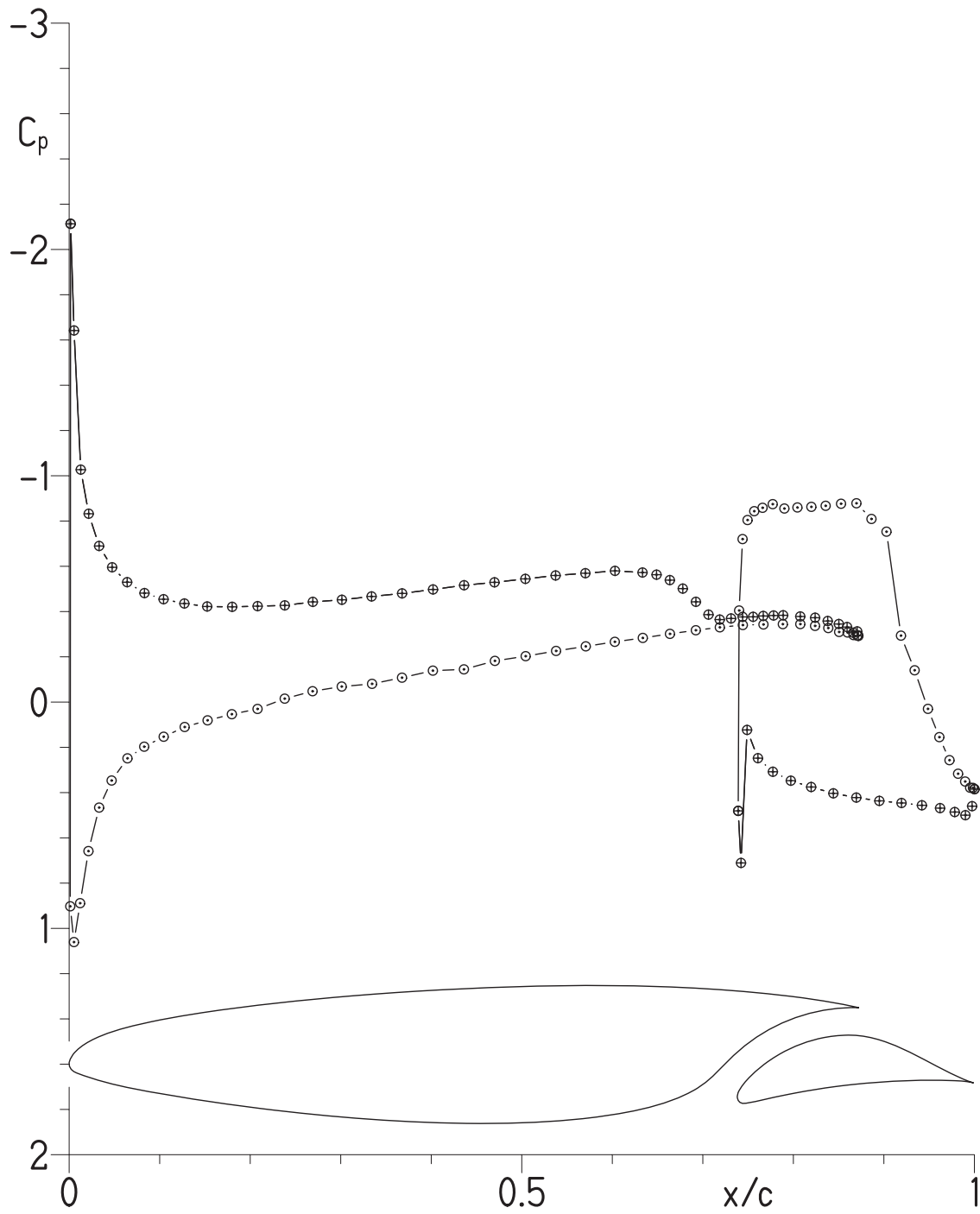
(a) $\alpha = -4.15°$; $c_l = -0.099$; $c_d = 0.0105$; $c_m = -0.135$.

Figure 4.- Pressure distributions for $R = 3.0 \times 10^6$ and $M = 0.10$ with transition free. Open symbols represent data for upper surface; crossed symbols, data for lower surface.
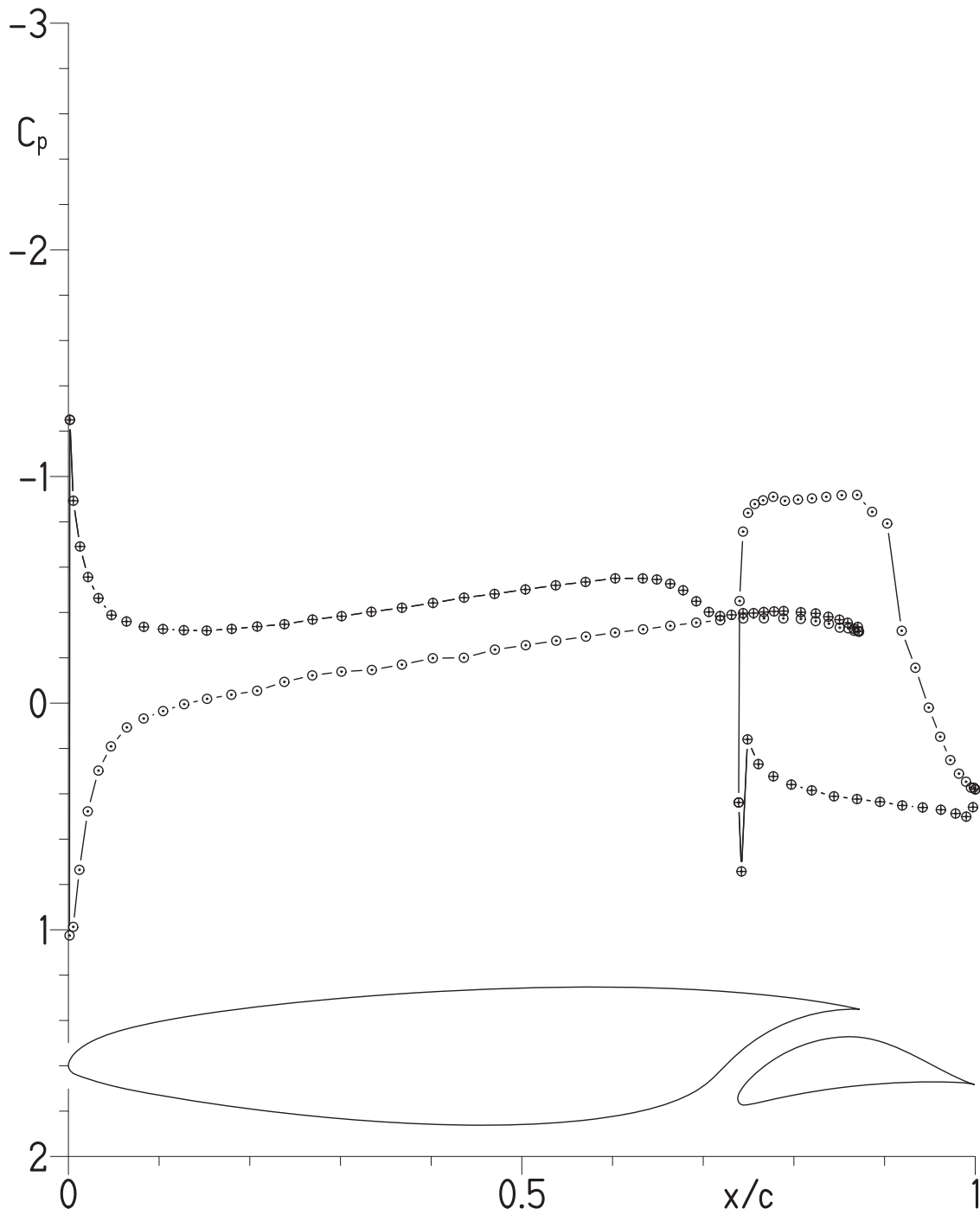
(b) $\alpha = -3.12°$; $c_l = 0.019$; $c_d = 0.0099$; $c_m = -0.139$.

Figure 4.- Continued.
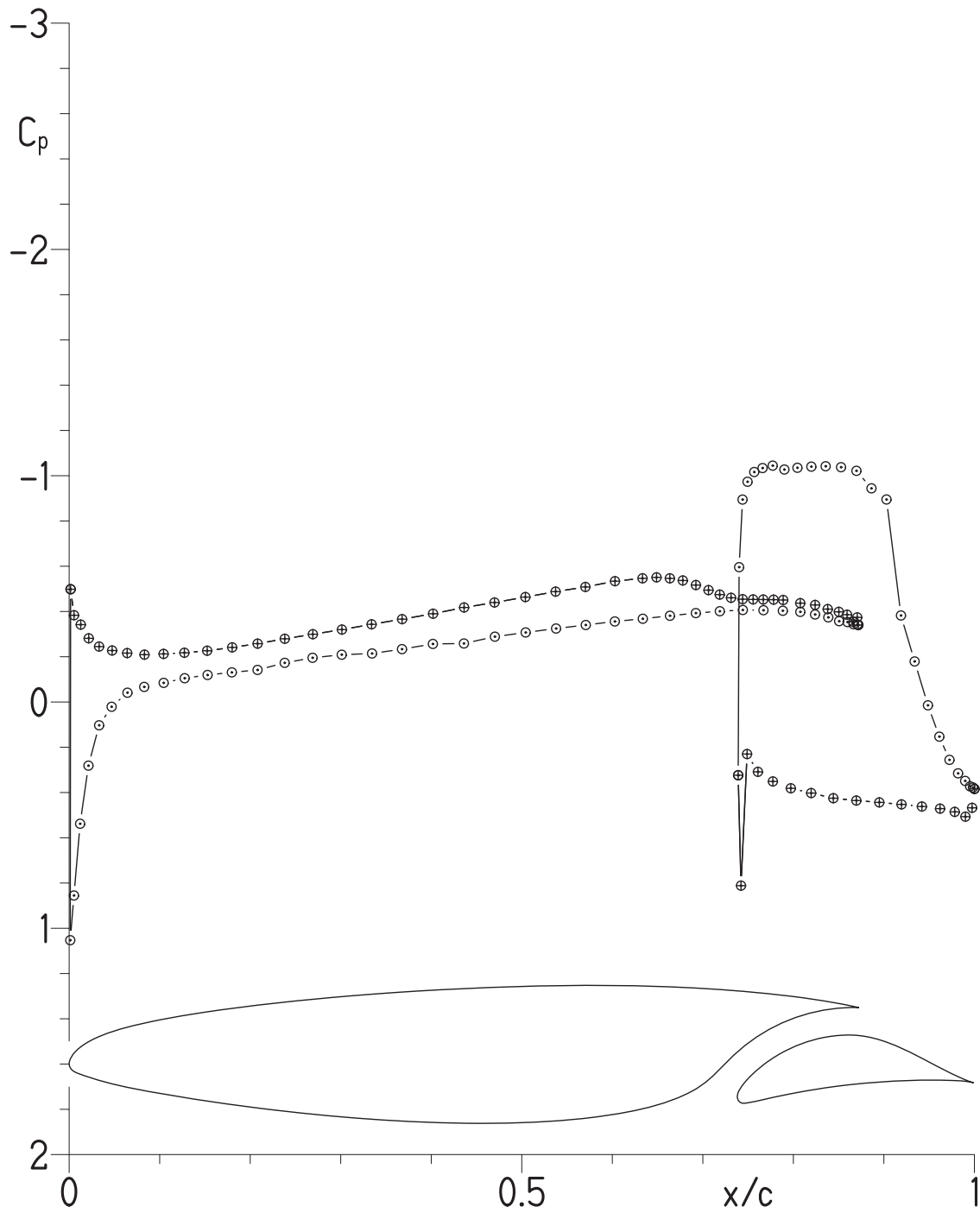
(c) $\alpha = -2.10°$; $c_l = 0.141$; $c_d = 0.054$; $c_m = -0.149$.

Figure 4.- Continued.
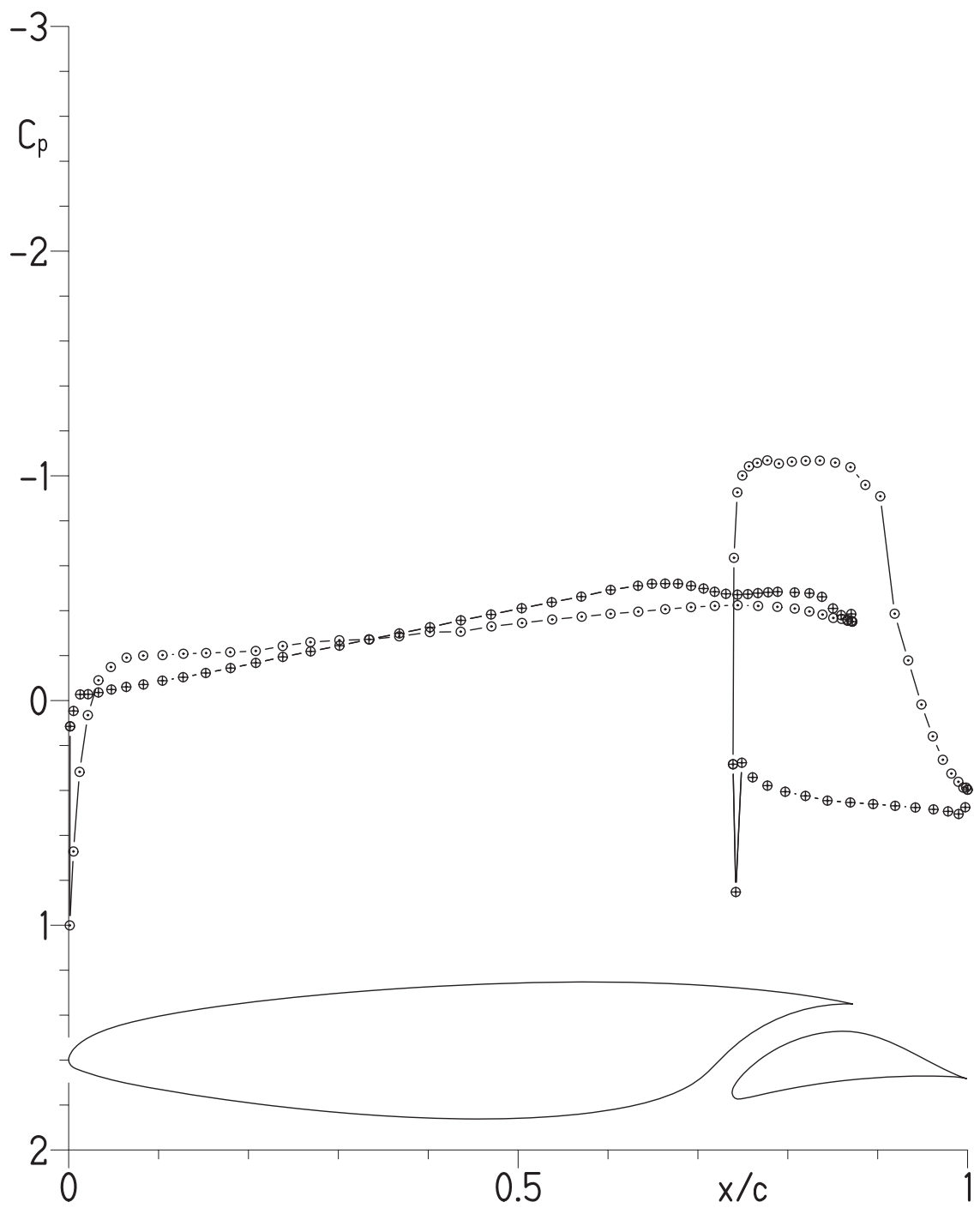
(d) $\alpha = -1.07°$; $c_l = 0.253$; $c_d = 0.0051$; $c_m = -0.150$.

Figure 4.- Continued.
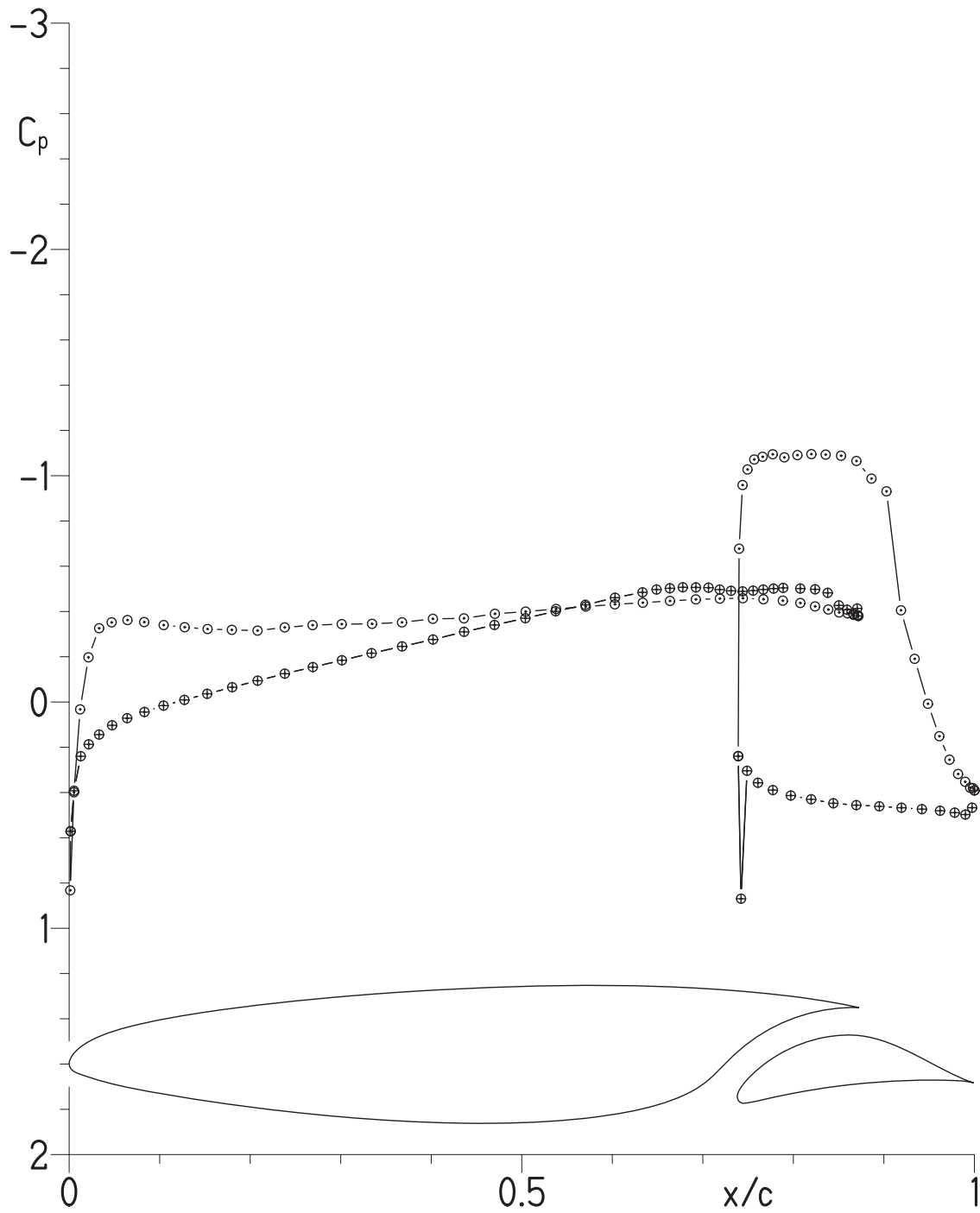
(e) $\alpha = -0.05°$; $c_l = 0.368$; $c_d = 0.0051$; $c_m = -0.153$.

Figure 4.- Continued.
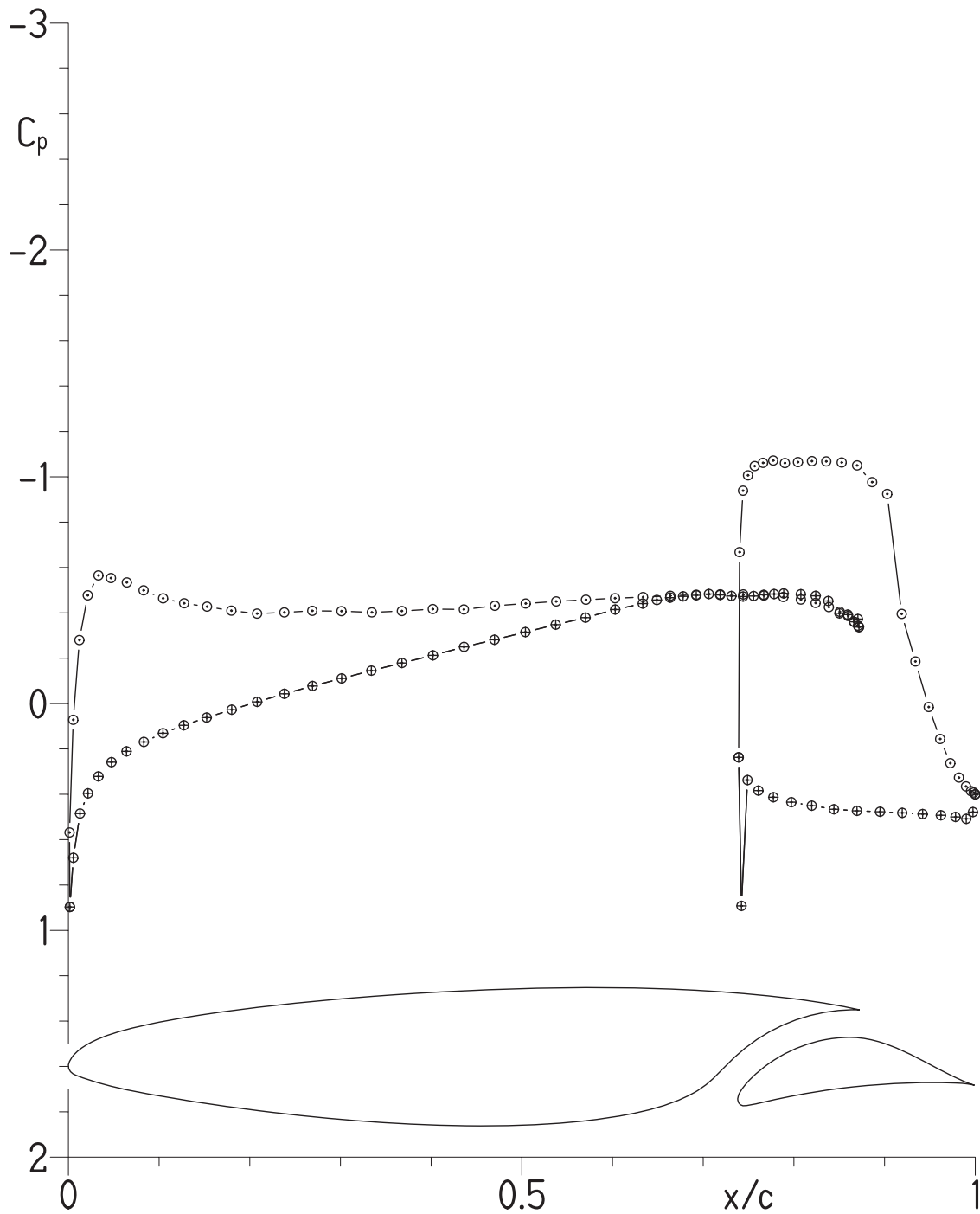
(f) $\alpha = 0.97°$; $c_l = 0.482$; $c_d = 0.0051$; $c_m = -0.156$.

Figure 4.- Continued.
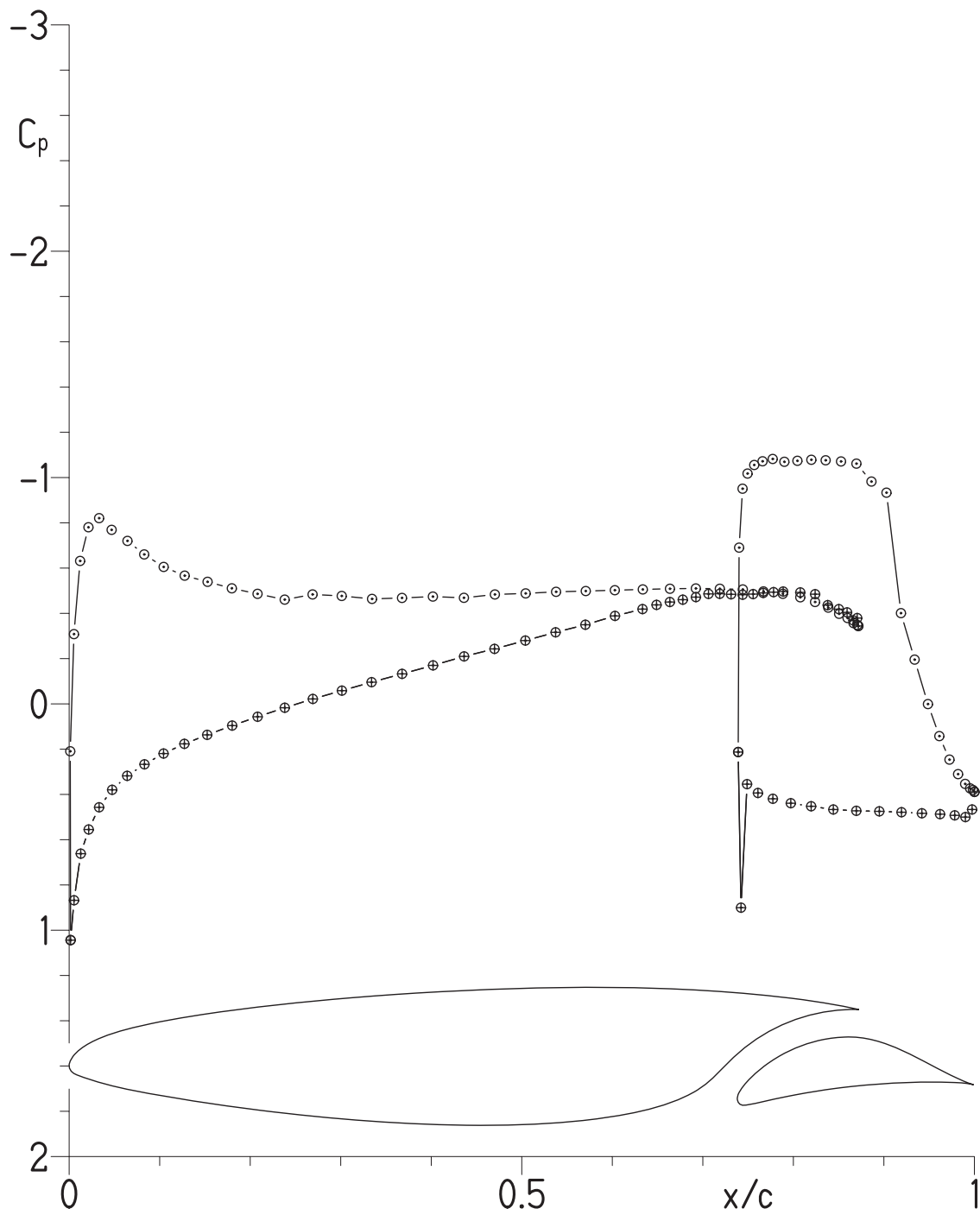
(g) $\alpha = 1.99°$; $c_l = 0.583$; $c_d = 0.0091$; $c_m = -0.155$.

Figure 4.- Continued.
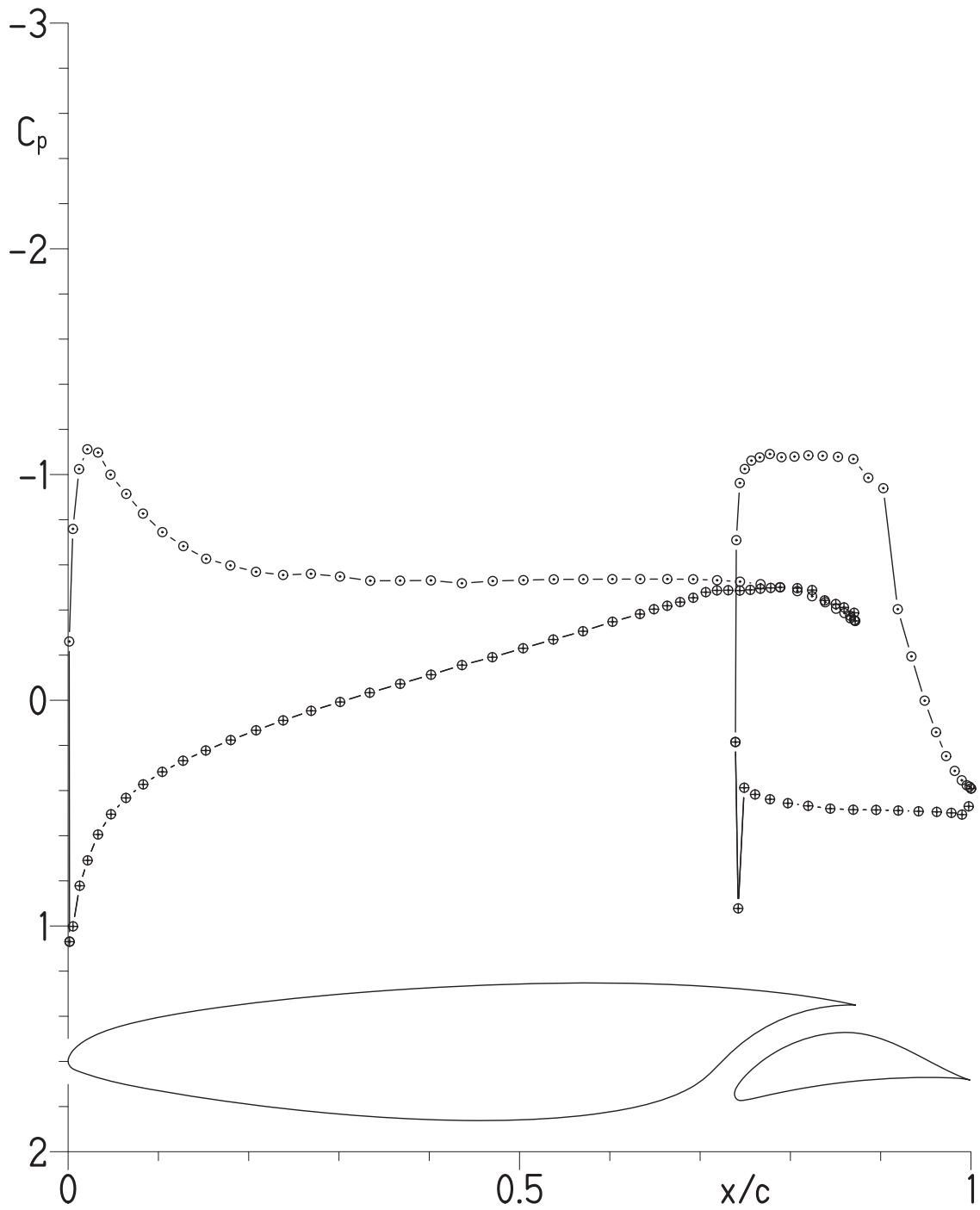
(h) $\alpha = 3.01°$; $c_l = 0.694$; $c_d = 0.0101$; $c_m = -0.157$.

Figure 4.- Continued.
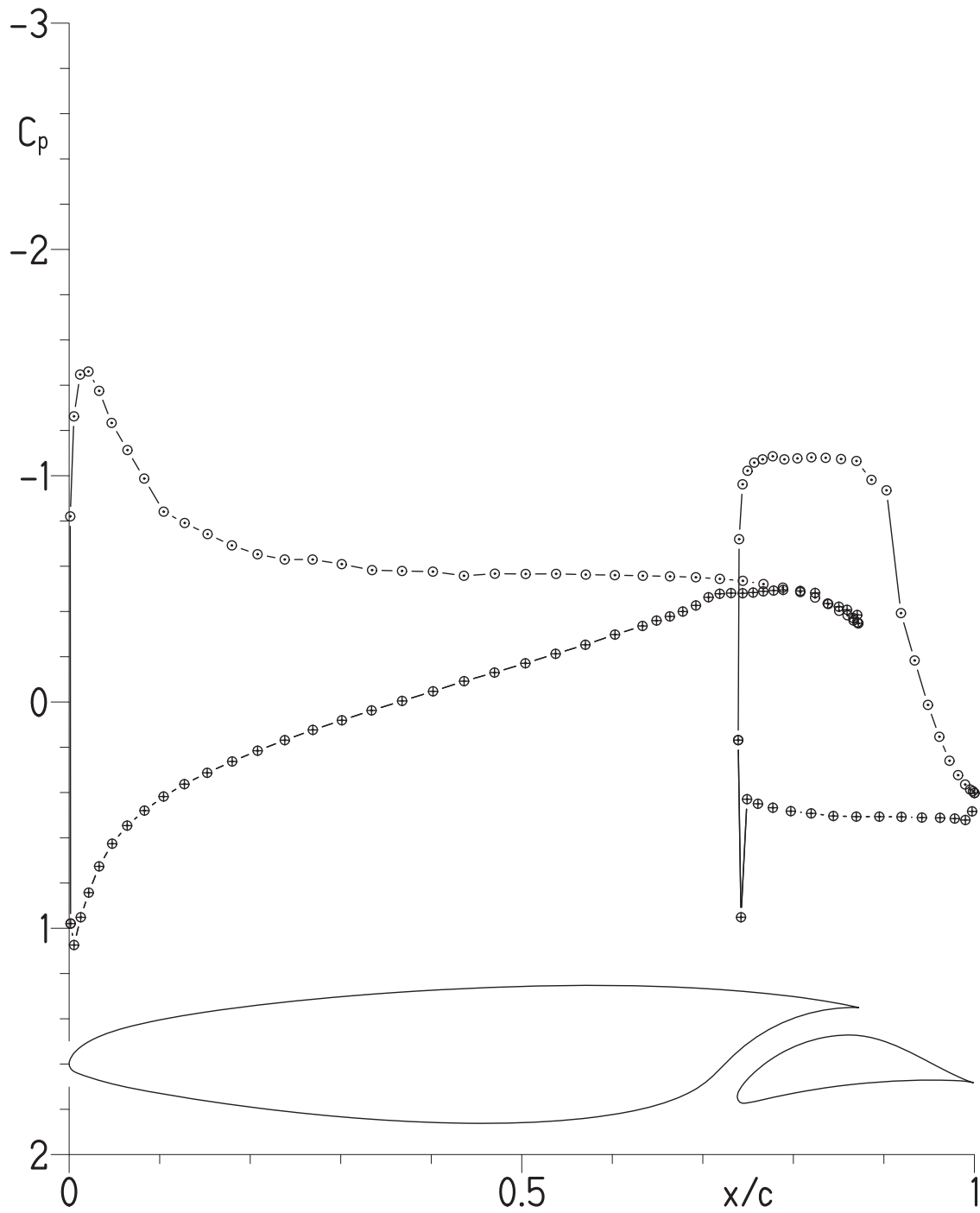
(i) $\alpha = 4.04°$; $c_l = 0.804$; $c_d = 0.0109$; $c_m = -0.159$.

Figure 4.- Continued.
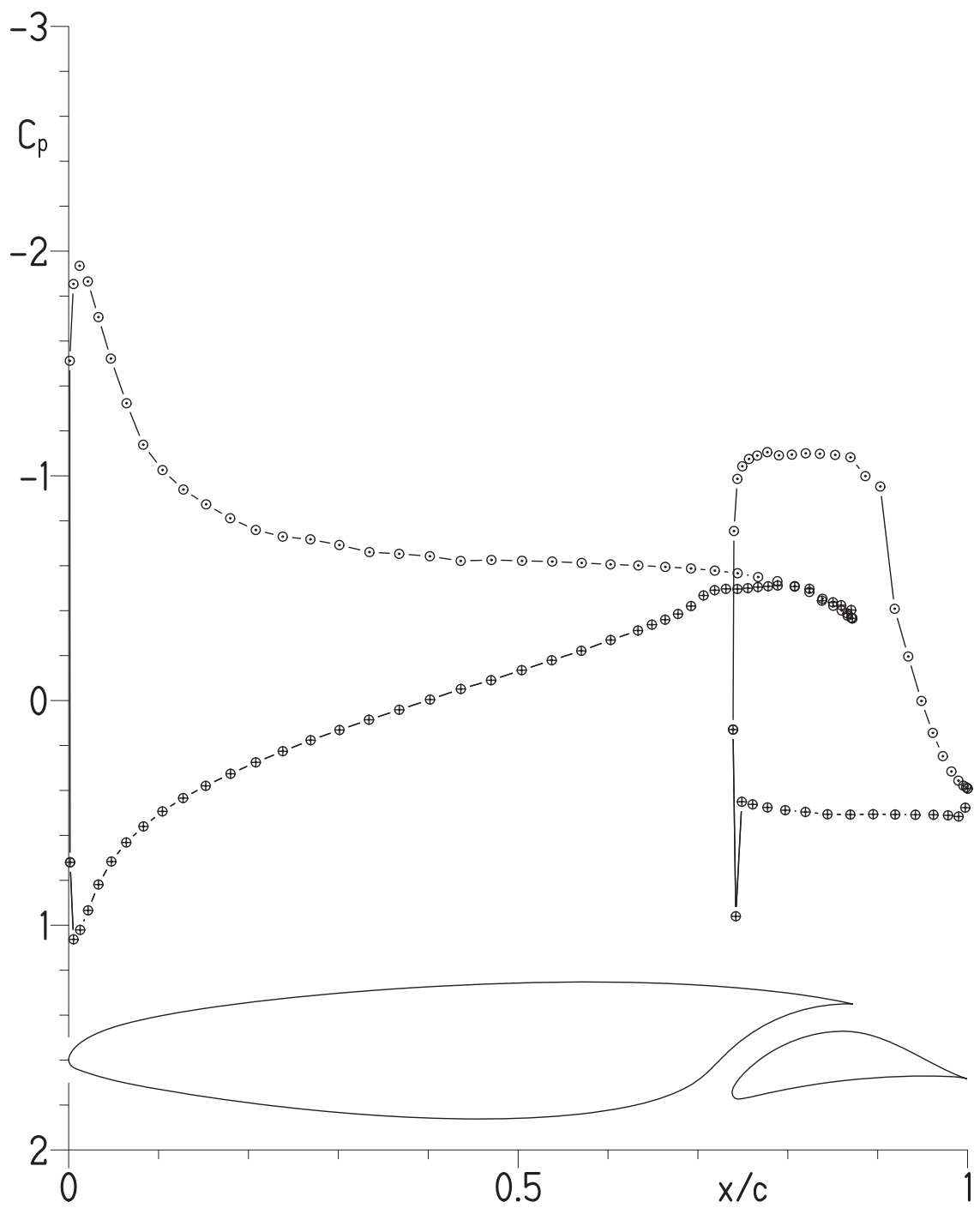
(j) $\alpha = 5.06°$; $c_l = 0.916$; $c_d = 0.0116$; $c_m = -0.161$.

Figure 4.- Continued.
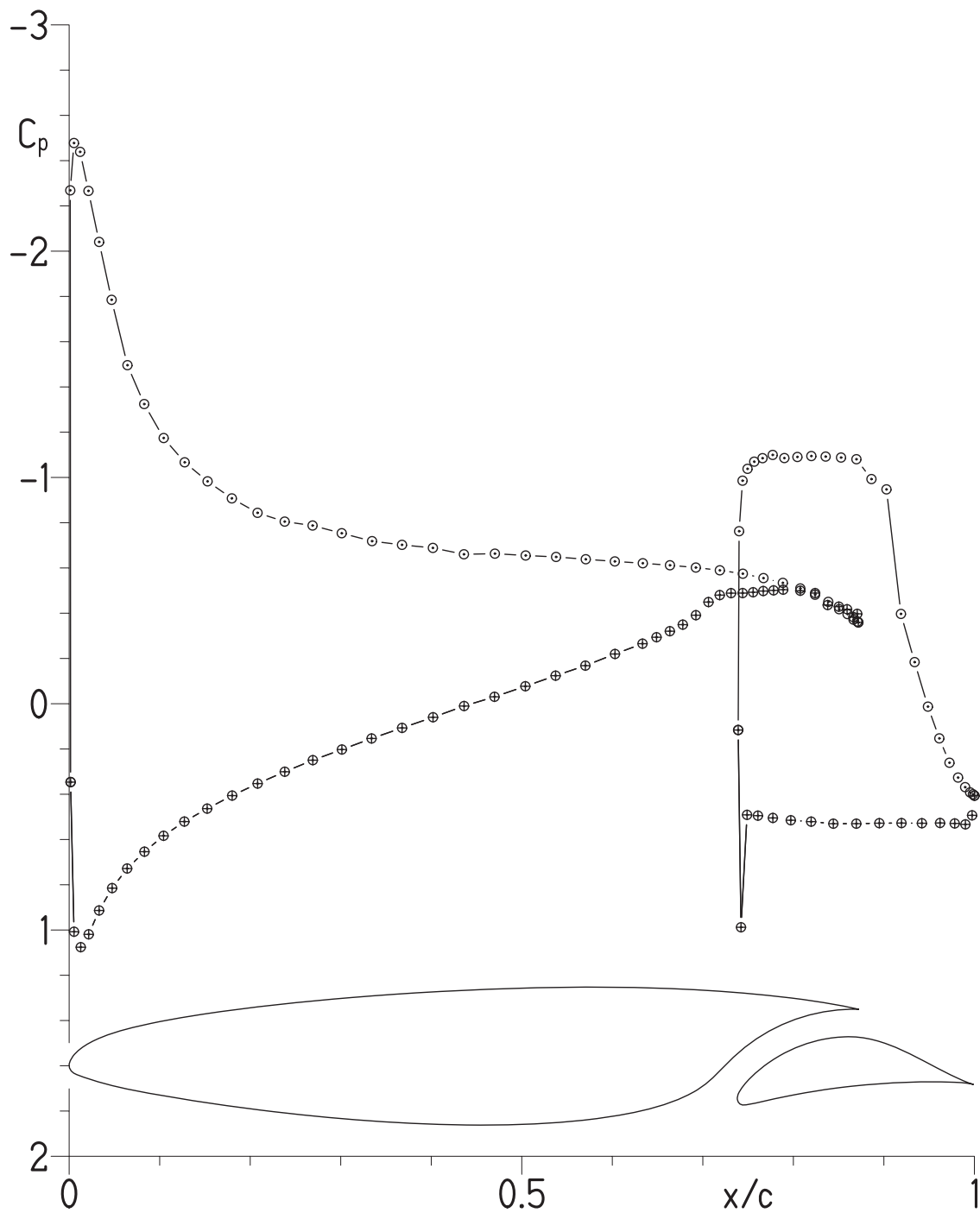
(k) $\alpha = 6.07°$; $c_l = 1.027$; $c_d = 0.0124$; $c_m = -0.163$.

Figure 4.- Continued.
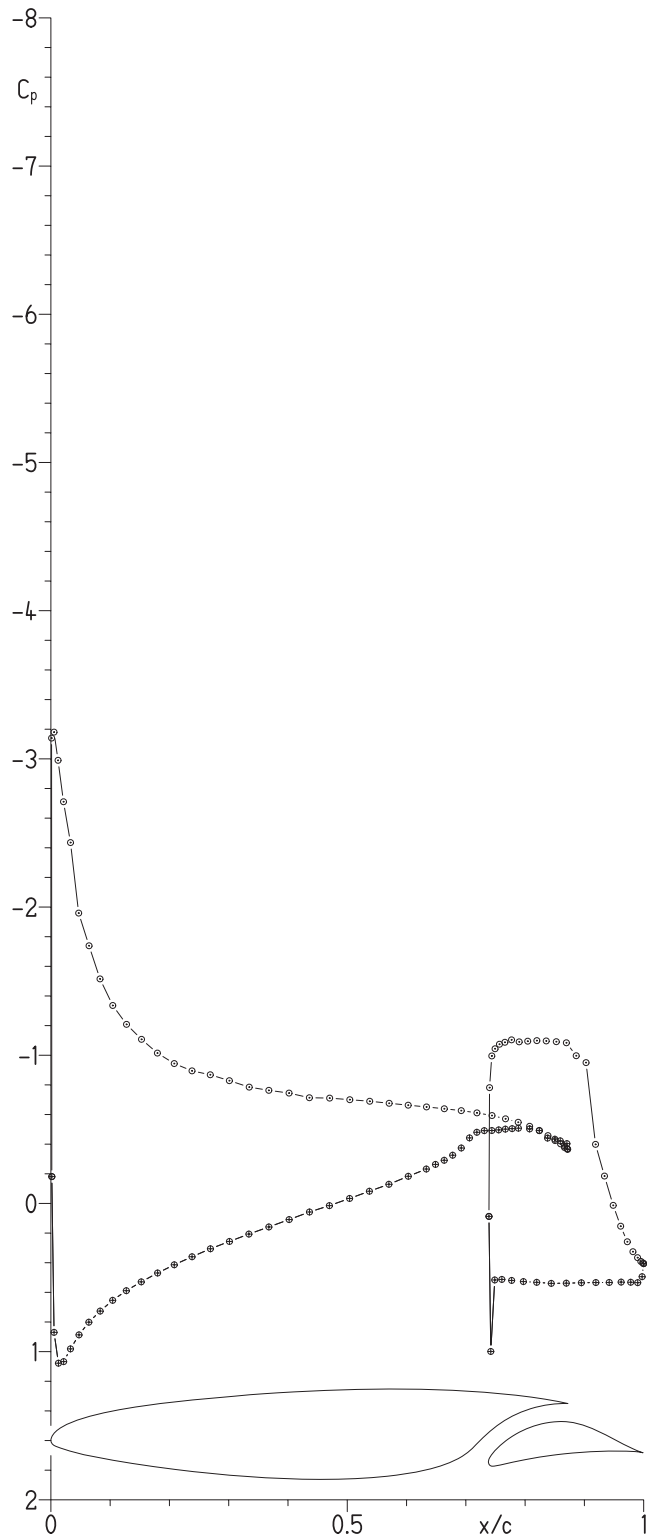
(l) $\alpha = 7.10°$; $c_l = 1.134$; $c_d = 0.0133$; $c_m = -0.164$.

Figure 4.- Continued.
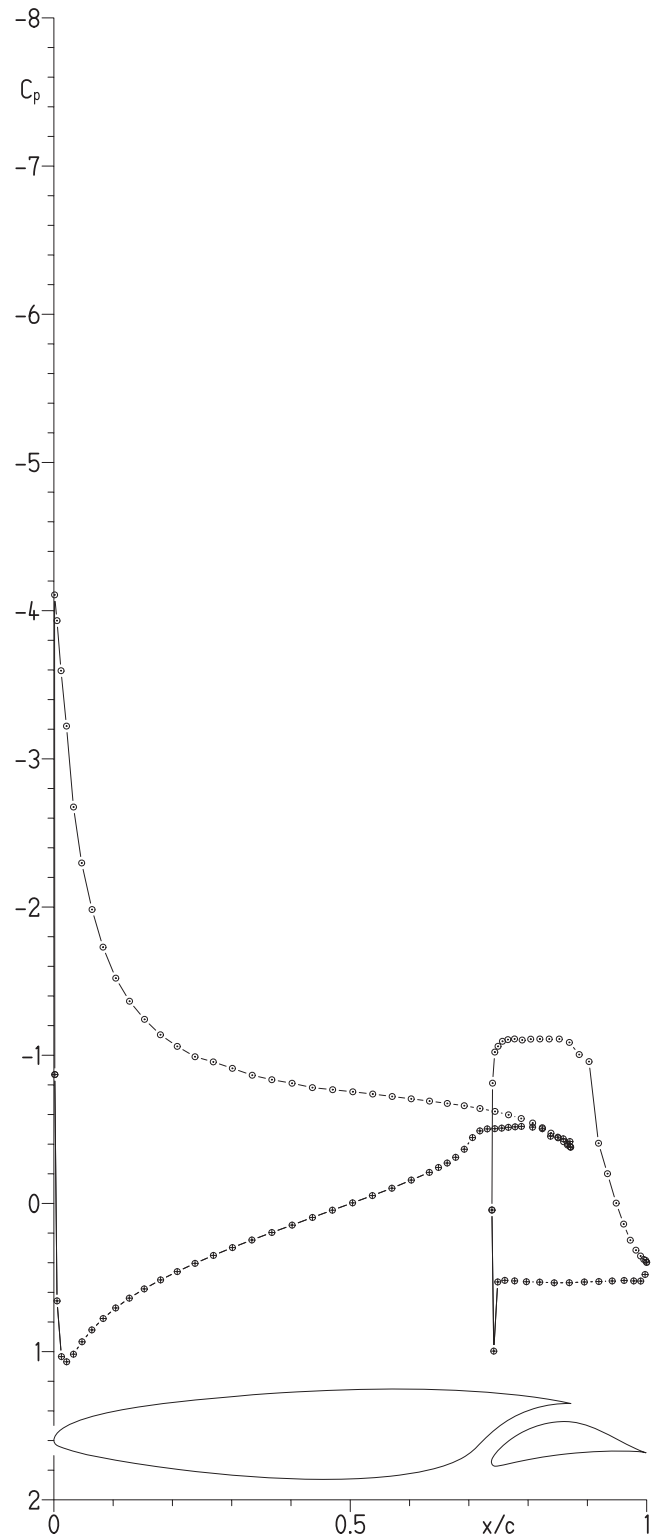
(m) $\alpha = 8.12°$; $c_l = 1.239$; $c_d = 0.0142$; $c_m = -0.165$.

Figure 4.- Continued.
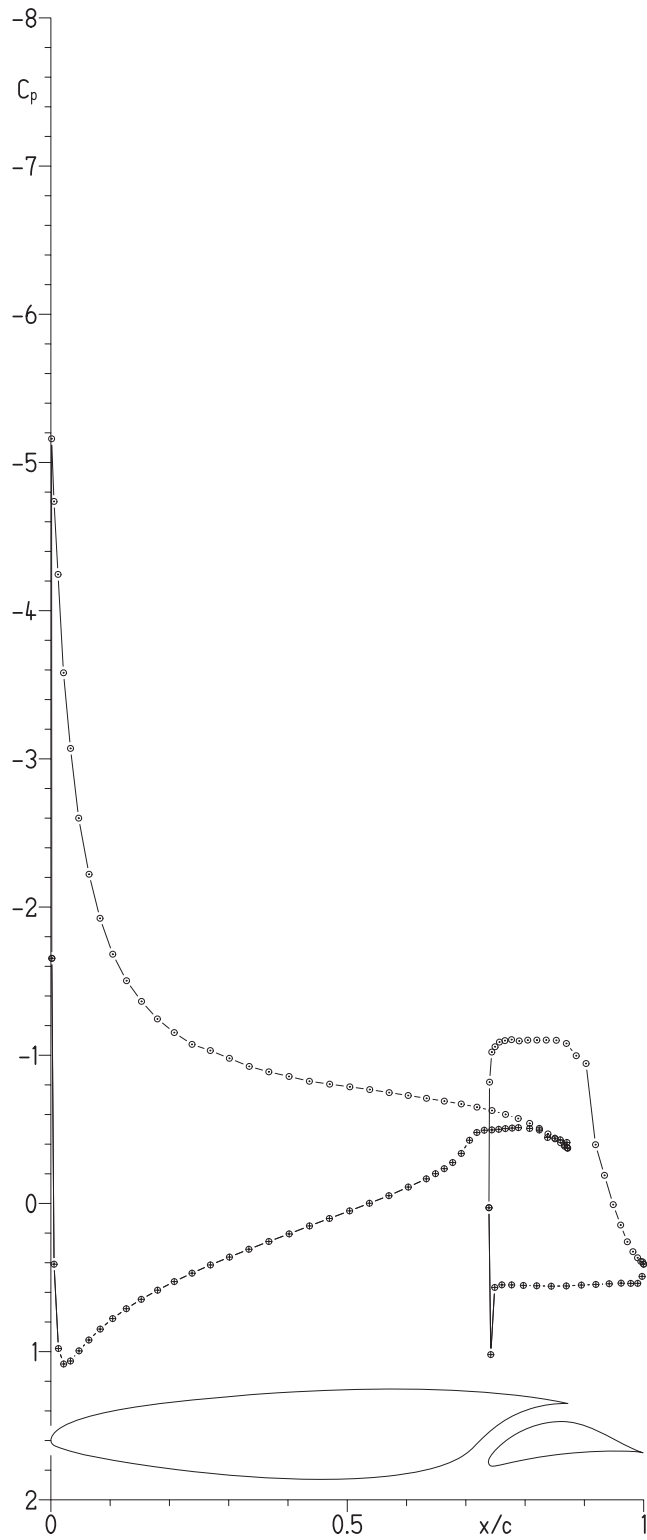
(n) $\alpha = 9.15°$; $c_l = 1.348$; $c_d = 0.0154$; $c_m = -0.166$.

Figure 4.- Continued.
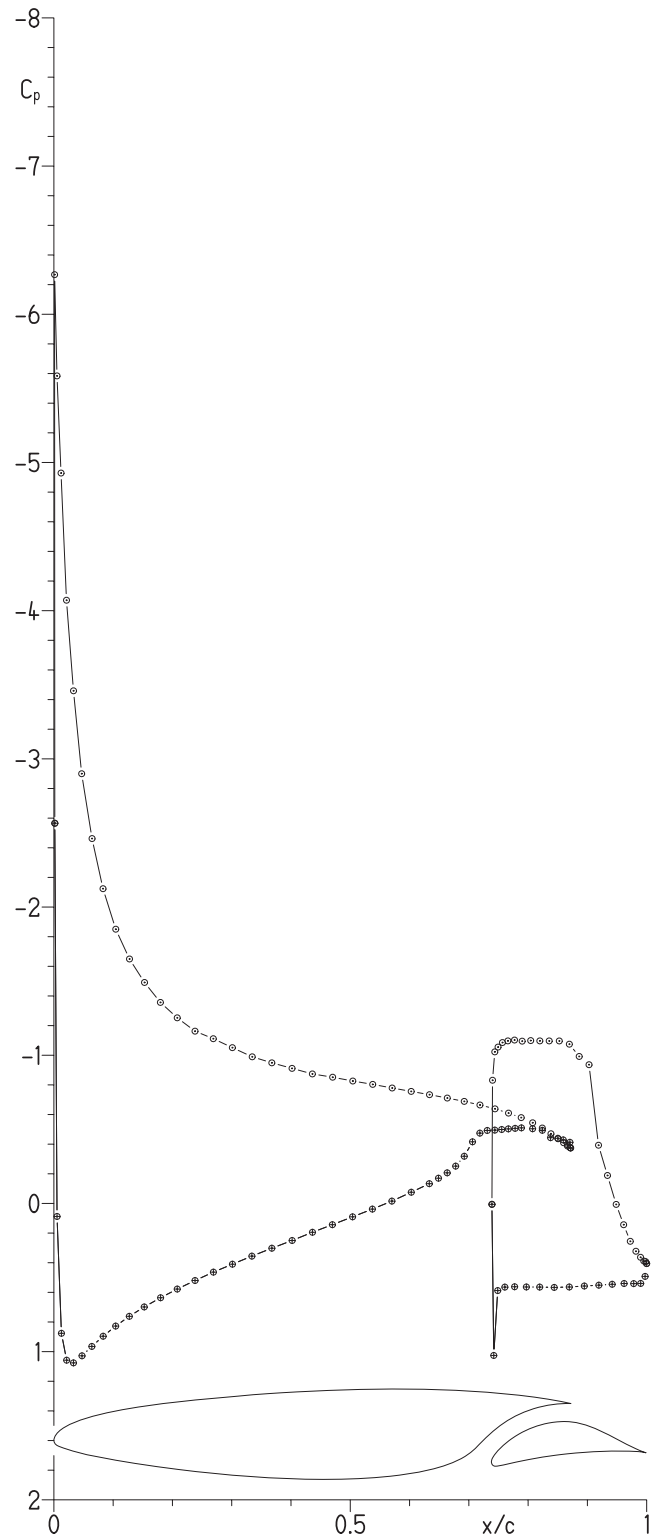
(o) $\alpha = 10.17°$; $c_l = 1.448$; $c_d = 0.0169$; $c_m = -0.165$.

Figure 4.- Continued.
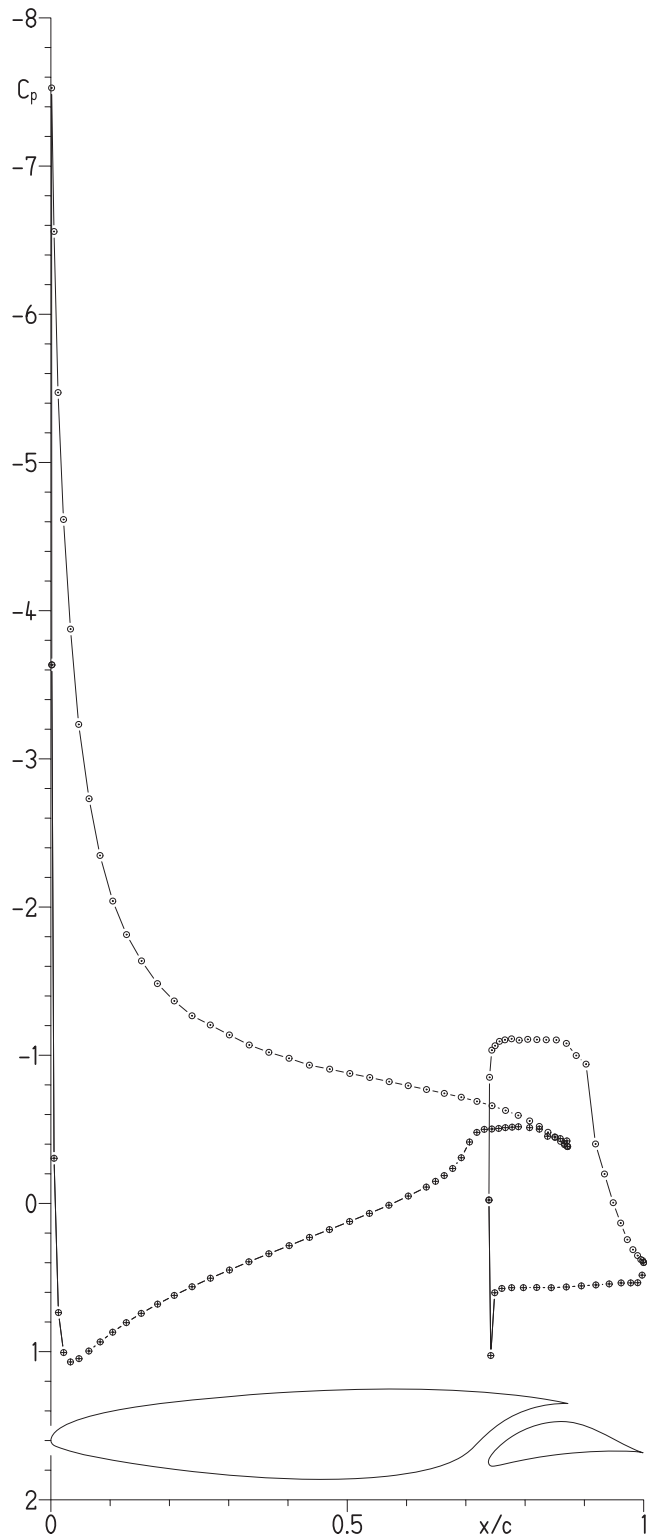
(p) $\alpha = 11.20°$; $c_l = 1.552$; $c_d = 0.0187$; $c_m = -0.165$.

Figure 4.- Continued.
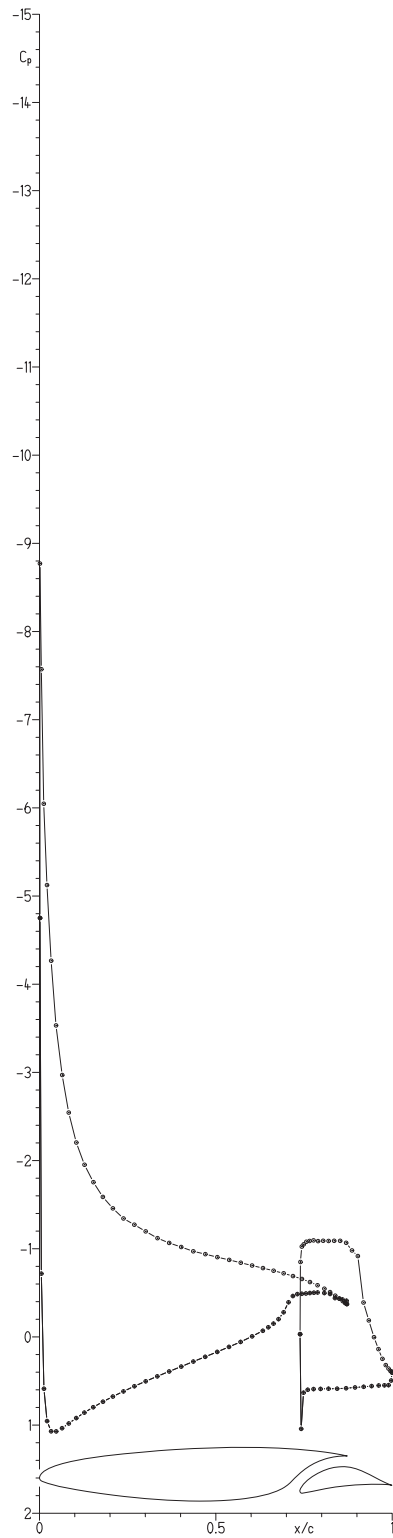
(q) $\alpha = 12.21°$; $c_l = 1.648$; $c_d = 0.0209$; $c_m = -0.165$.

Figure 4.- Continued.
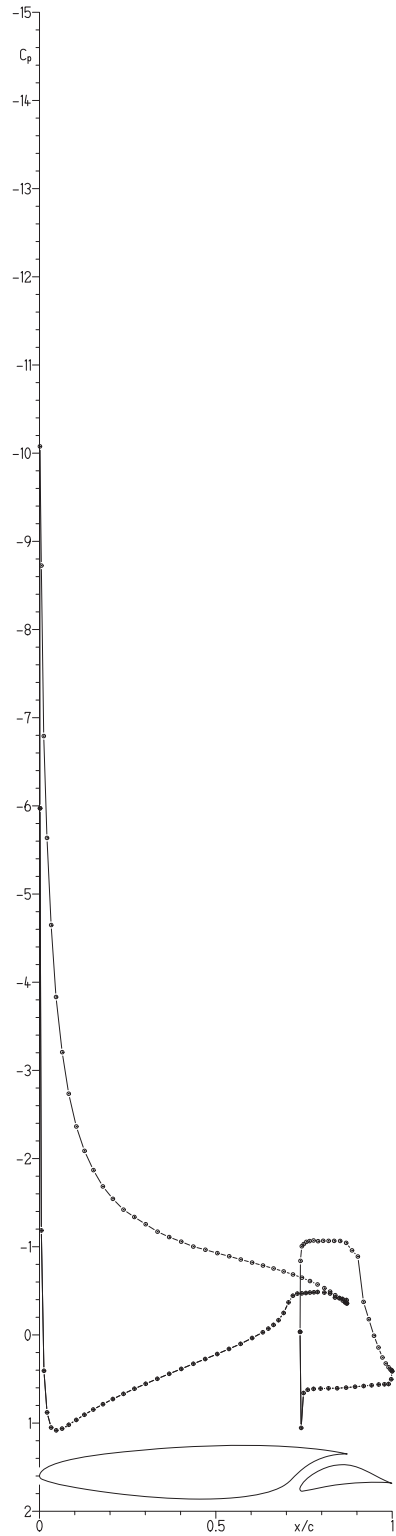
(r) $\alpha = 13.24°$; $c_l = 1.738$; $c_d = 0.0235$; $c_m = -0.162$.

Figure 4.- Continued.
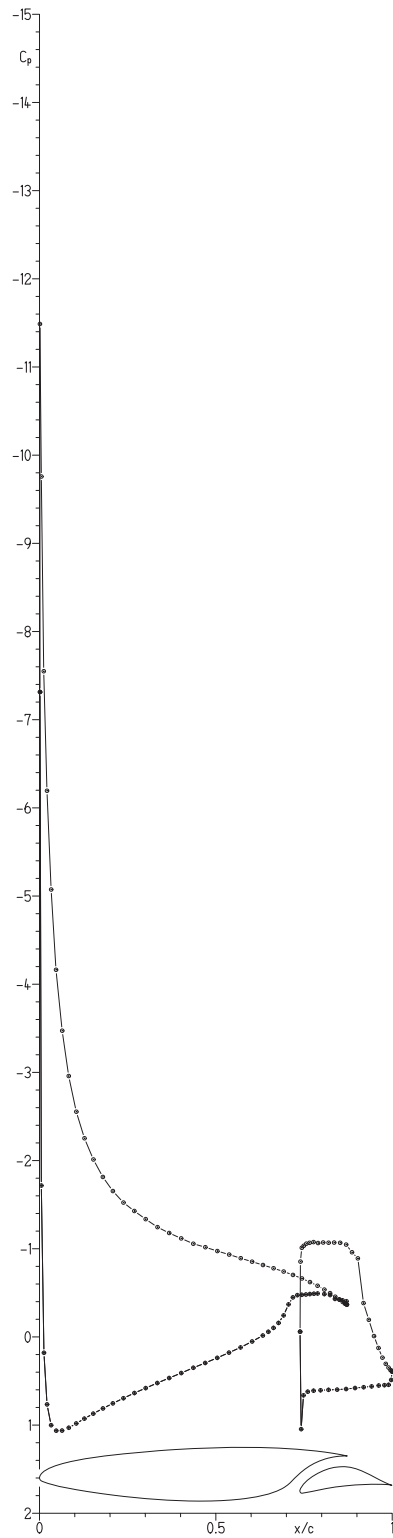
(s) $\alpha = 14.25°$; $c_l = 1.828$; $c_d = 0.0269$; $c_m = -0.160$.

Figure 4.- Continued.
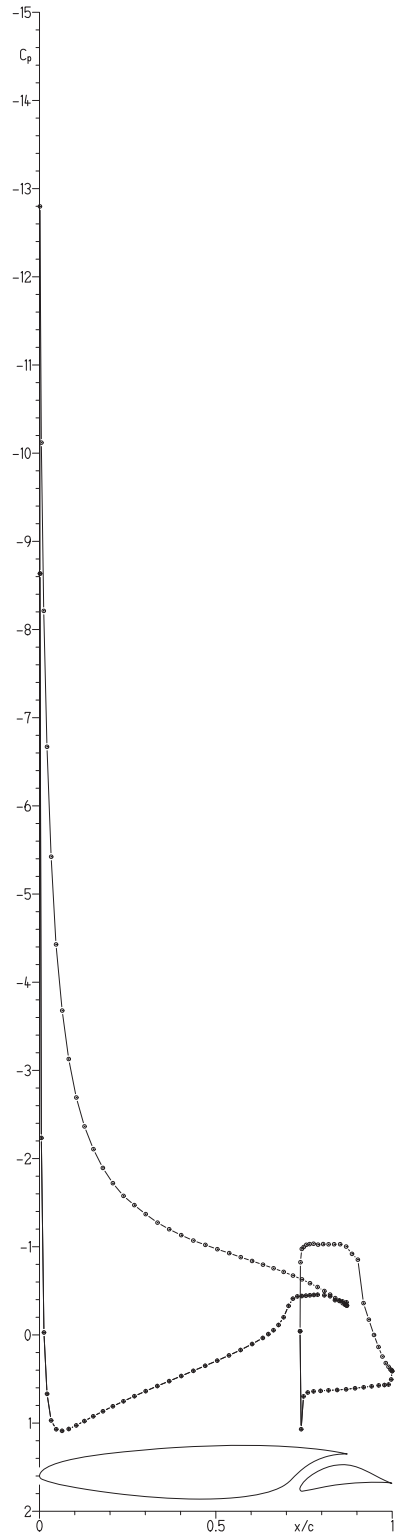
(t) $\alpha = 15.27°$; $c_l = 1.899$; $c_d = 0.0309$; $c_m = -0.158$.

Figure 4.- Continued.
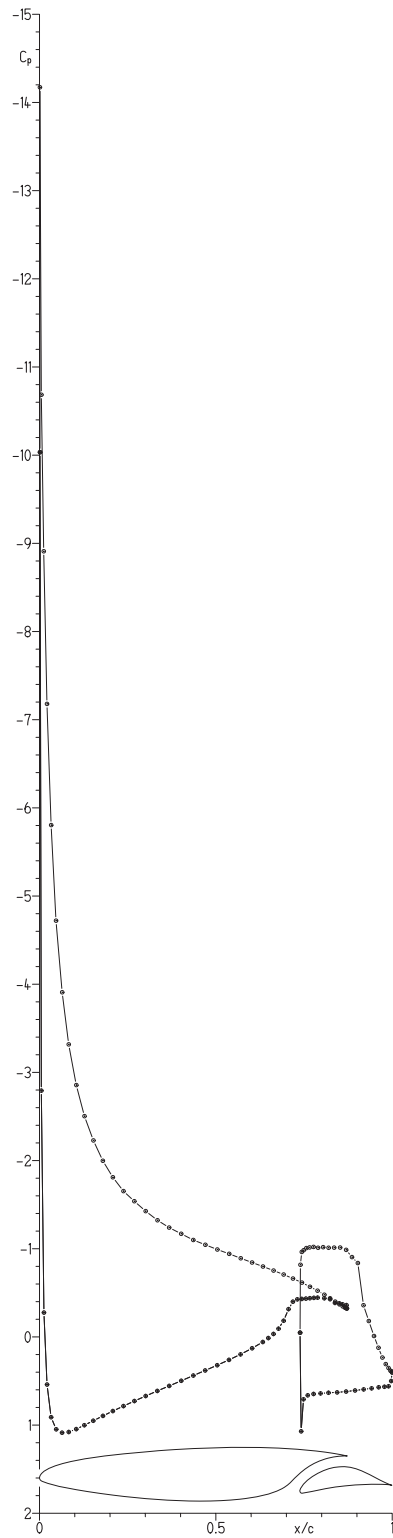
(u) $\alpha = 16.29°$; $c_l = 1.969$; $c_d = 0.0352$; $c_m = -0.154$.

Figure 4.- Continued.
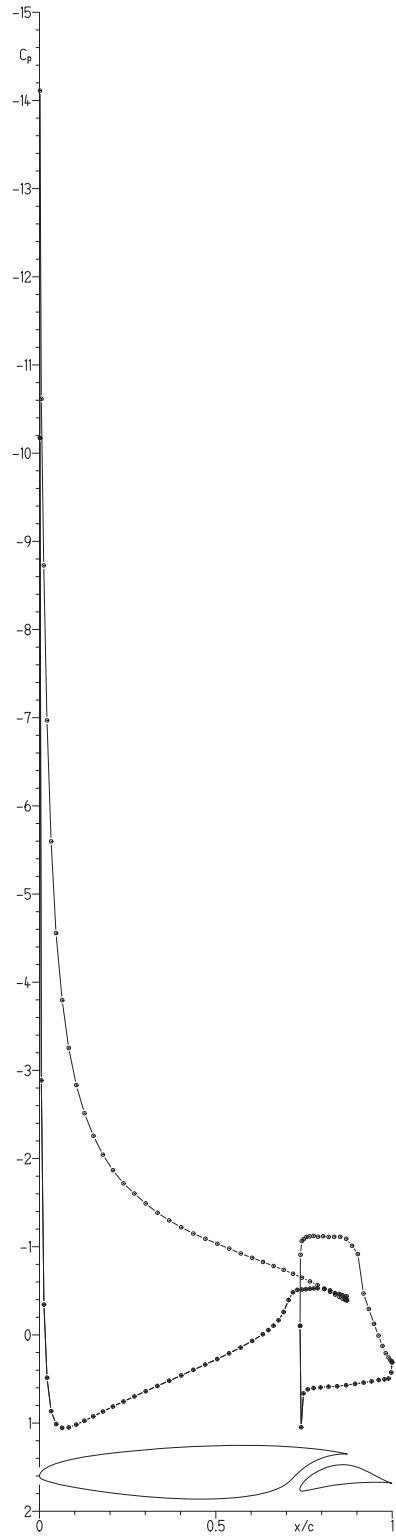
(v) $\alpha = 17.27°$; $c_l = 1.927$; $c_d = 0.1080$; $c_m = -0.158$.

Figure 4.- Continued.
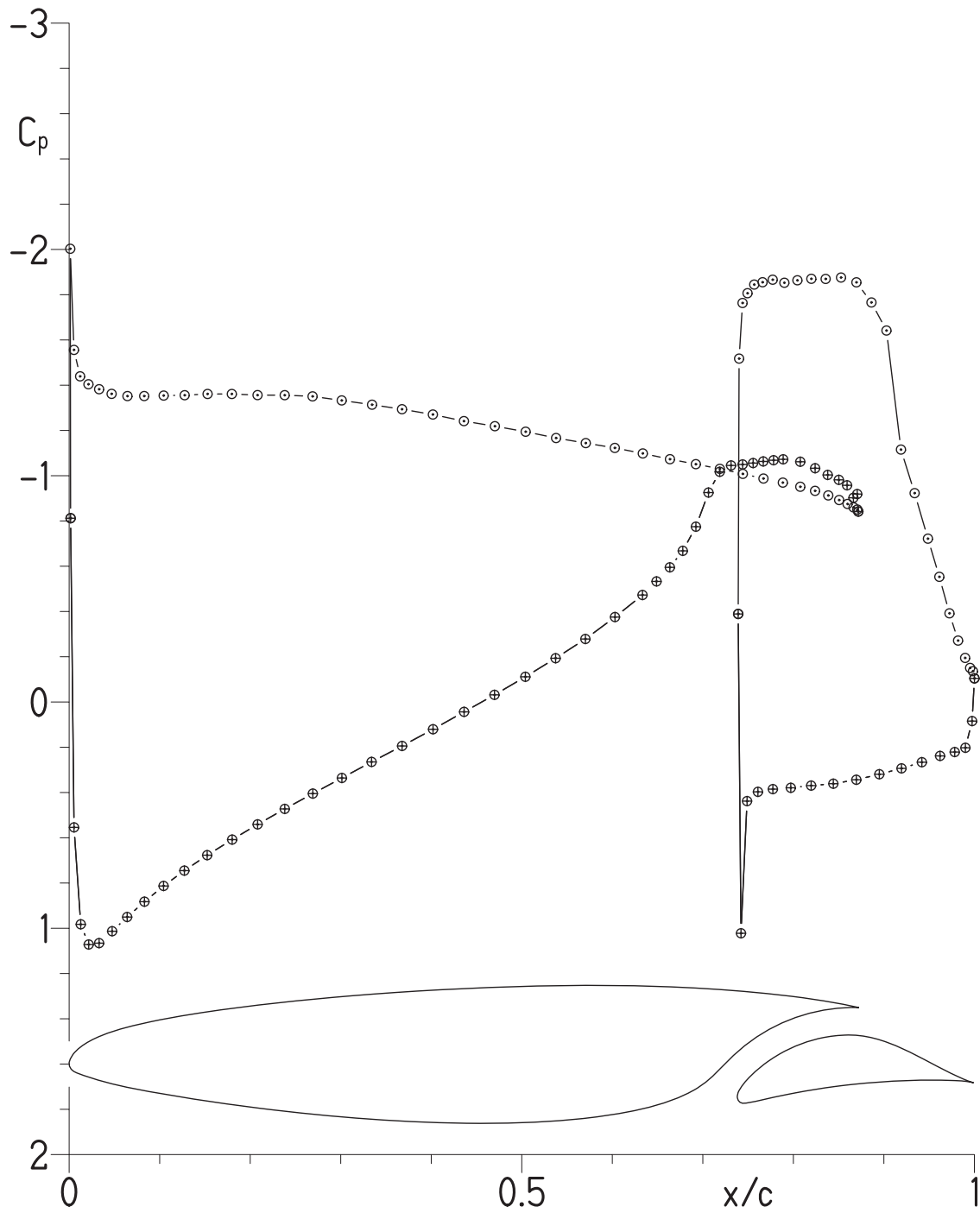
(w) $\alpha = 18.04°$; $c_l = 1.263$; $c_d = 0.3764$; $c_m = -0.255$.

Figure 4.- Concluded.
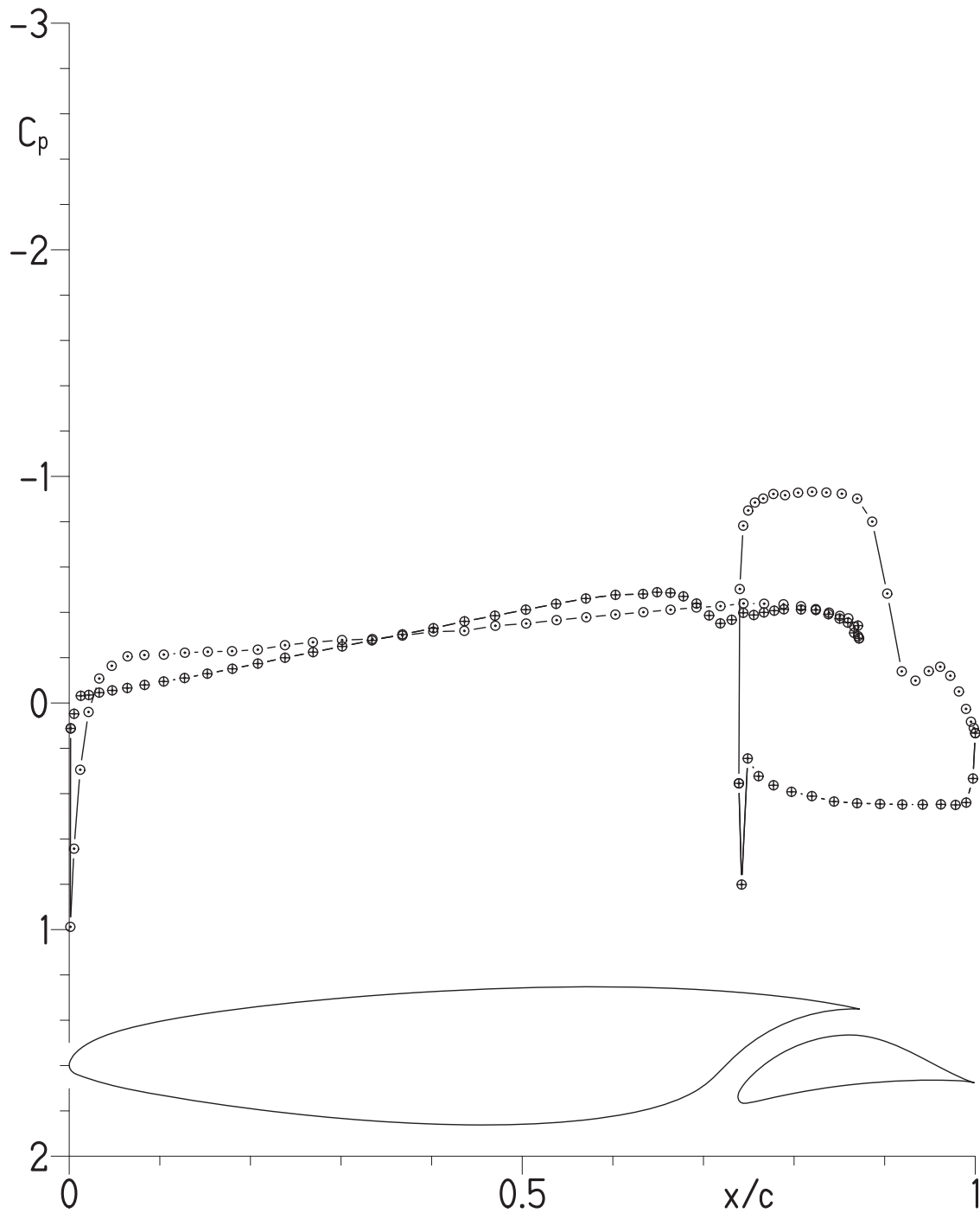
Figure 5.- Pressure distribution at $\alpha = -1.08°$ for $R = 9.1 \times 10^6$ and $M = 0.10$ with transition free. Open symbols represent data for upper surface; crossed symbols, data for lower surface.
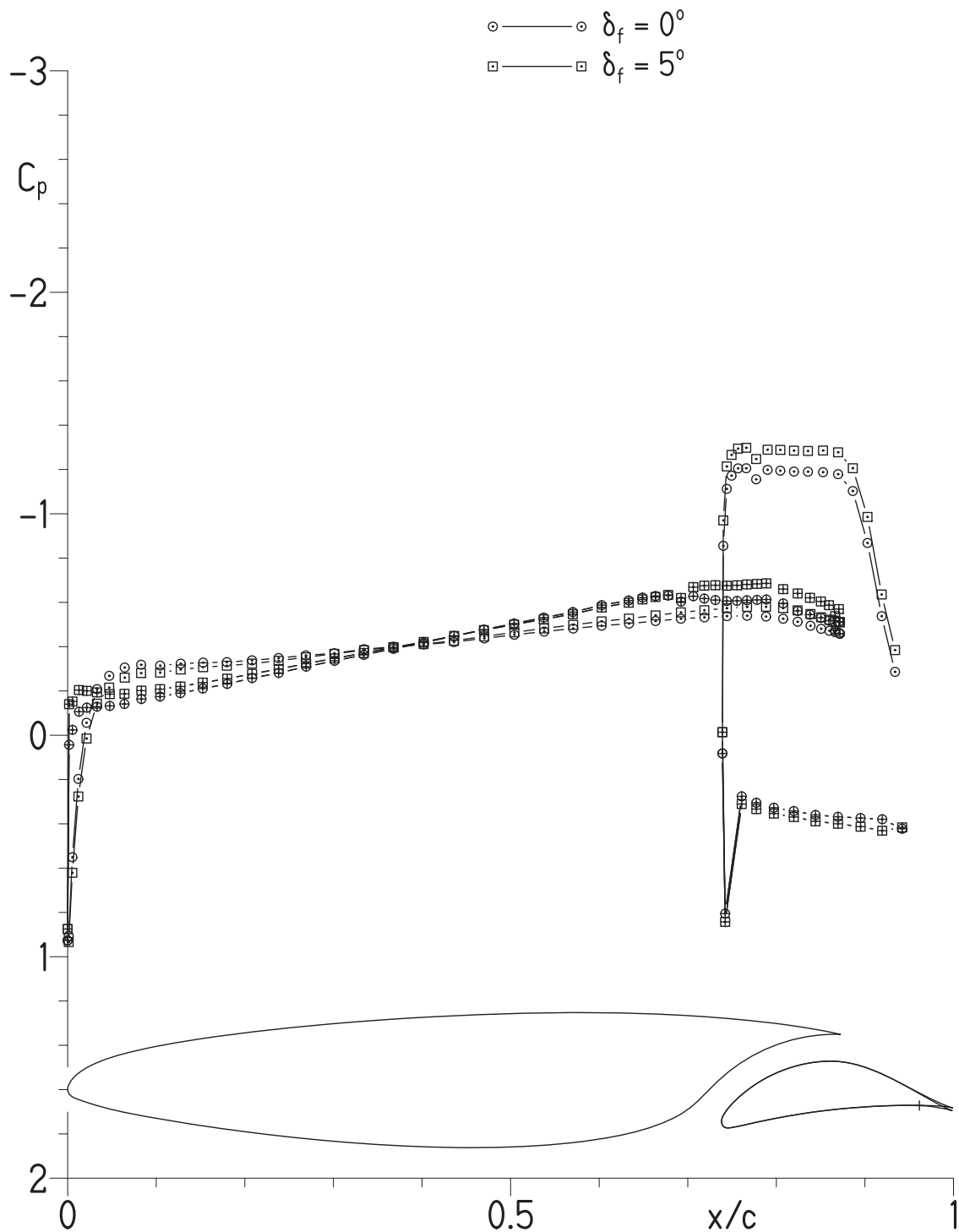
Figure 6.- Effect of aft-element flap deflection on pressure distribution at $c_l = 0.3$ for $R = 6 \times 10^6$ and $M = 0.1$ with transition free. Open symbols represent data for upper surface; crossed symbols, data for lower surface.
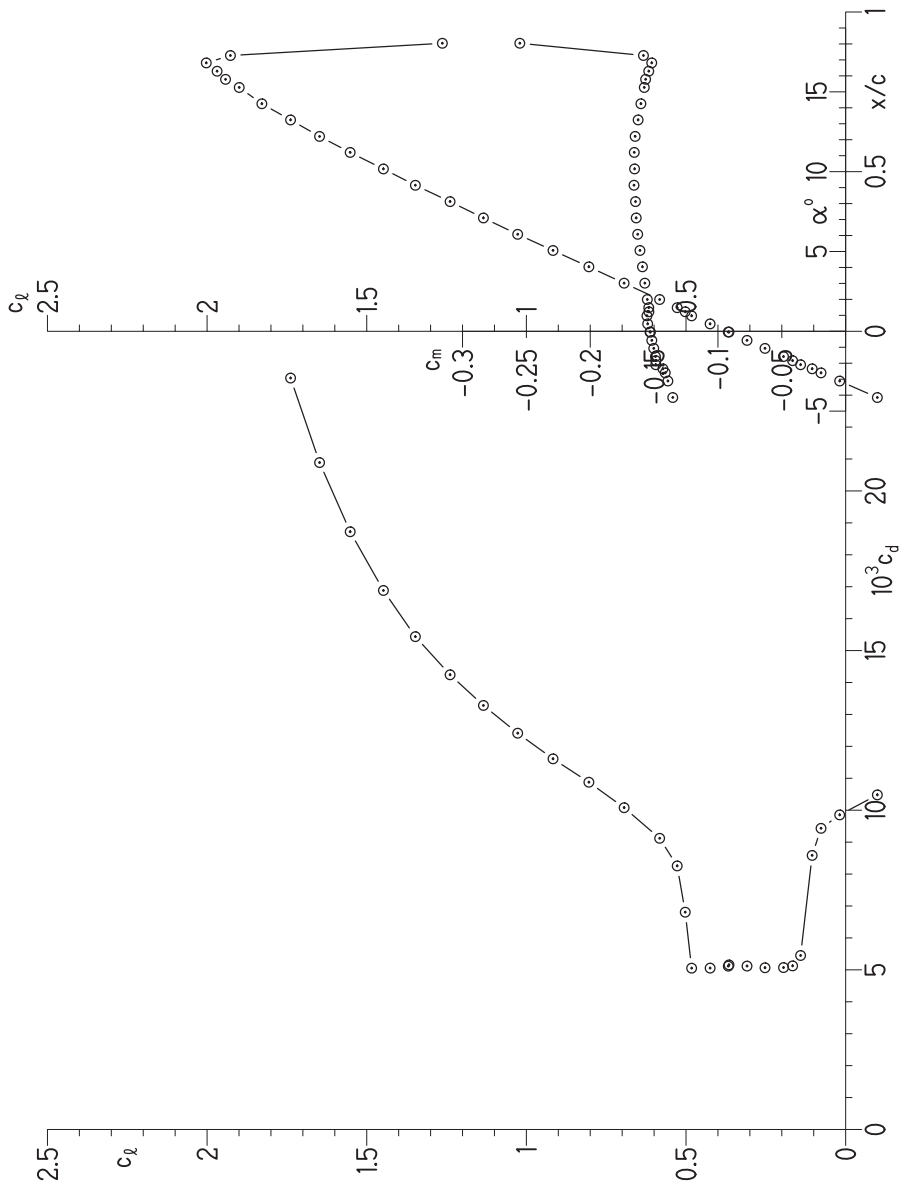
(a) $R = 3.0 \times 10^6$.

Figure 7.- Section characteristics at $M = 0.10$ with transition free.
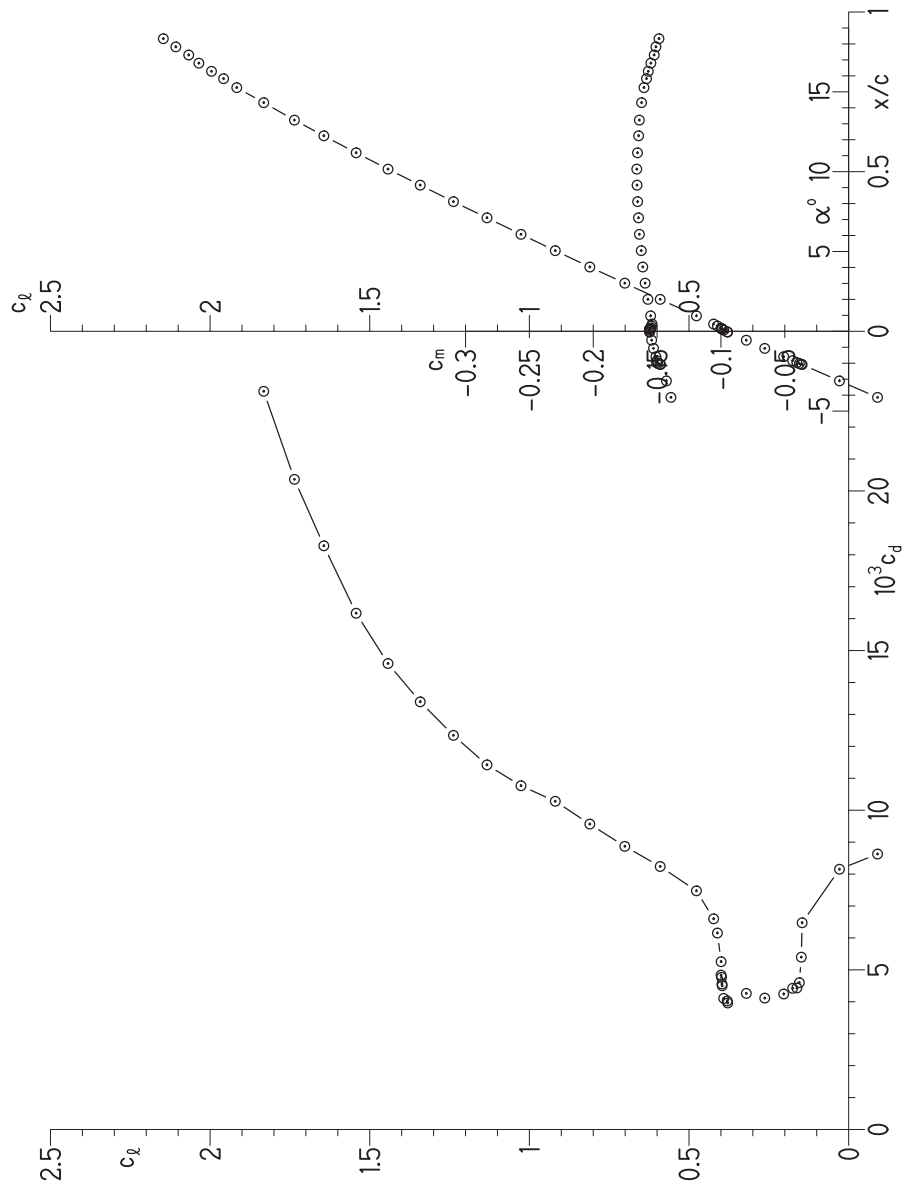
(b) R = 6.1 × 10⁶.

Figure 7.- Concluded.
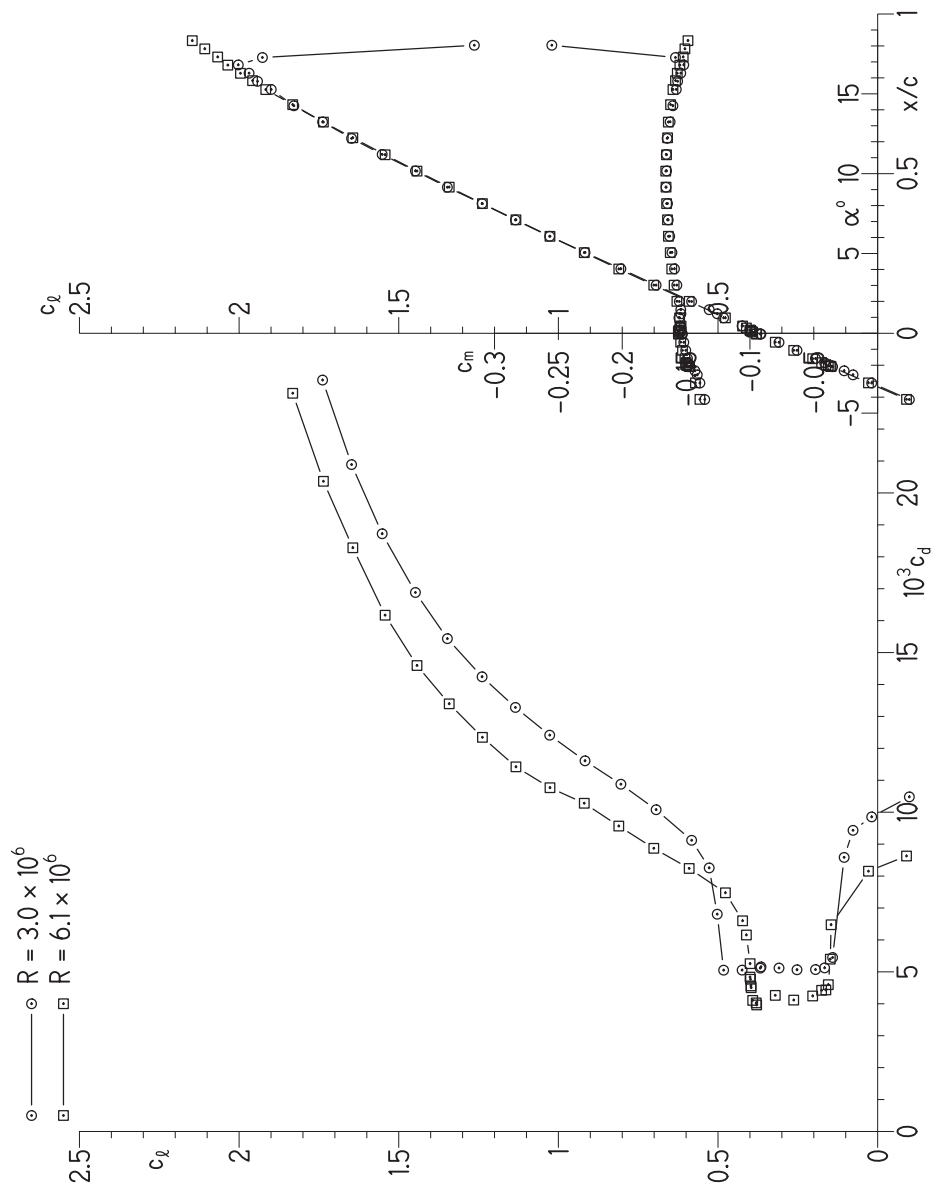
Figure 8.- Effect of Reynolds number on section characteristics at $M = 0.10$ with transition free.
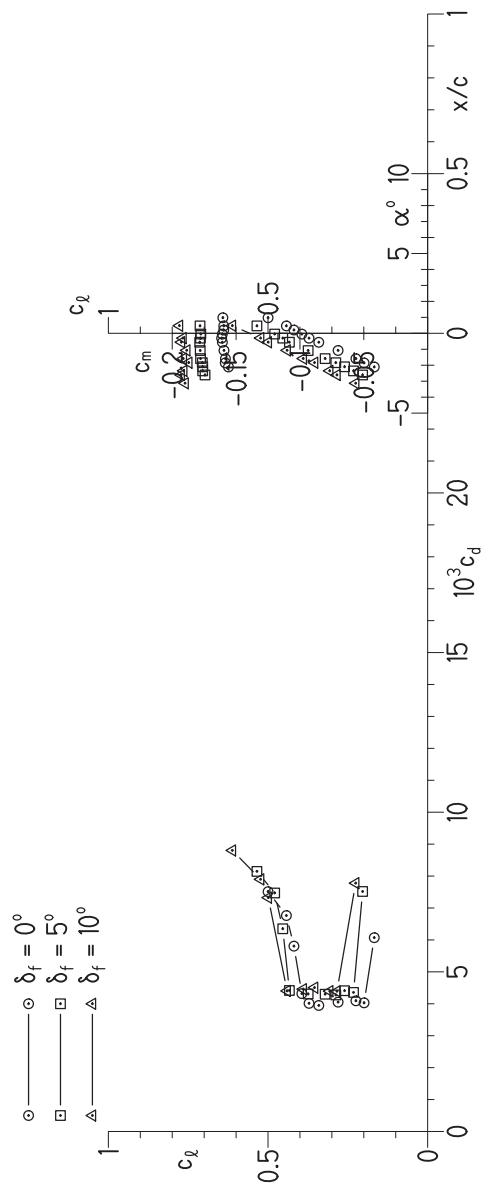
Figure 9.- Effect of aft-element flap deflection on section characteristics for $R = 6 \times 10^6$ and $M = 0.1$ with transition free.

(a) $\alpha = -3.12°$.

Figure 10.- Comparison of theoretical and experimental pressure distributions for $R = 3.0 \times 10^6$ and $M = 0.10$ with transition free. Open symbols represent data for upper surface; crossed symbols, data for lower surface.
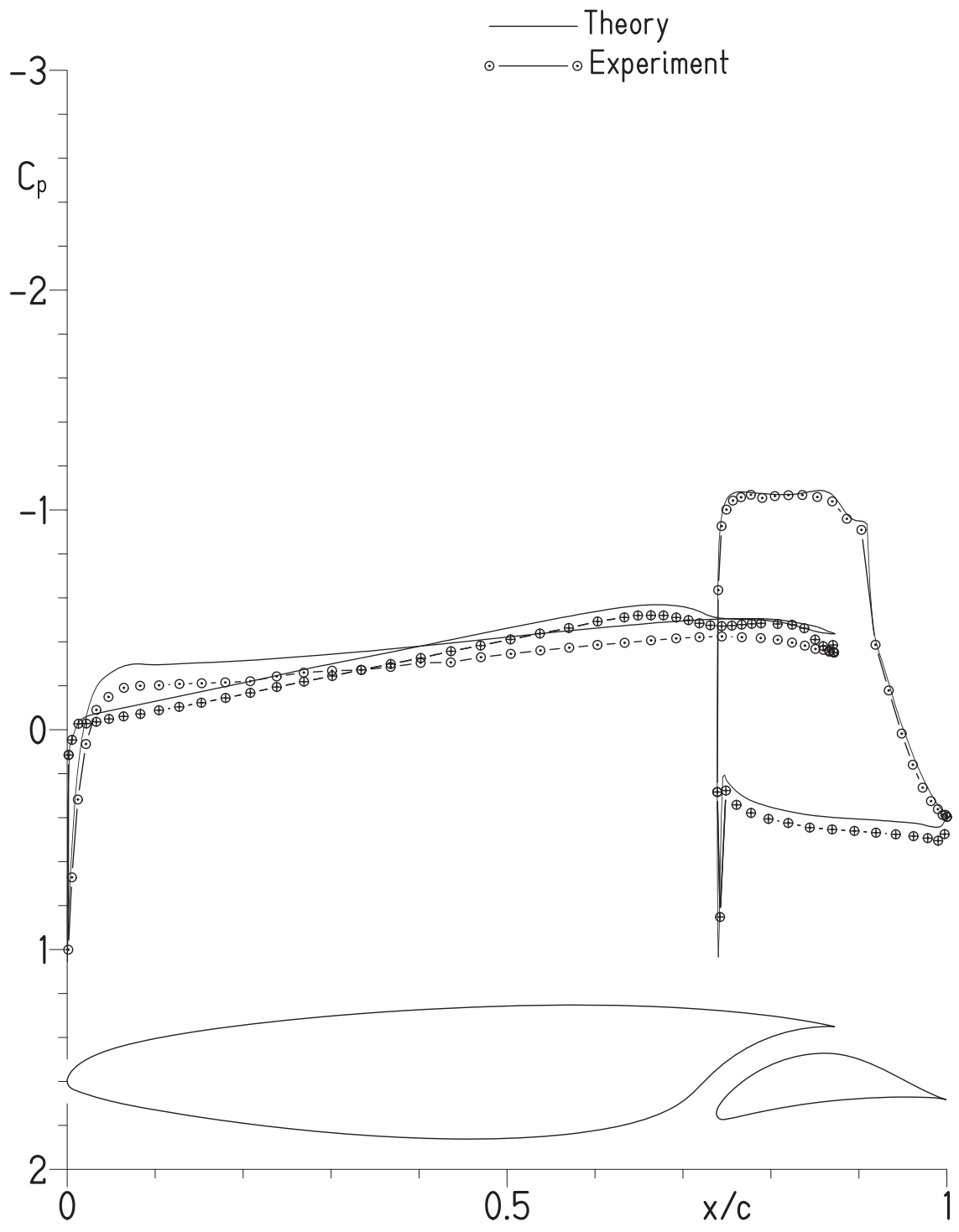
(b) $\alpha = -1.07°$.

Figure 10.- Continued.
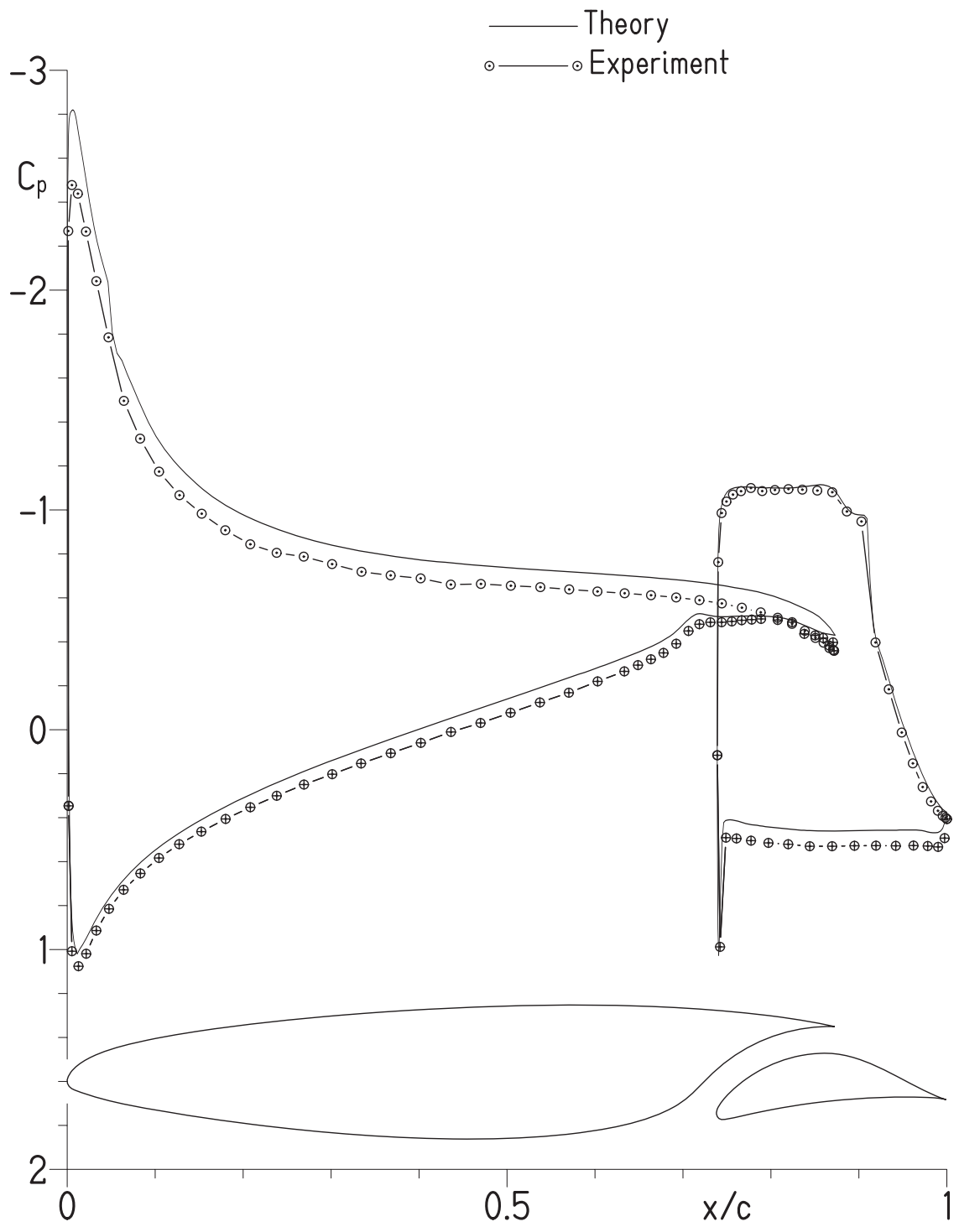
(c) $\alpha = 6.07°$.

Figure 10.- Continued.
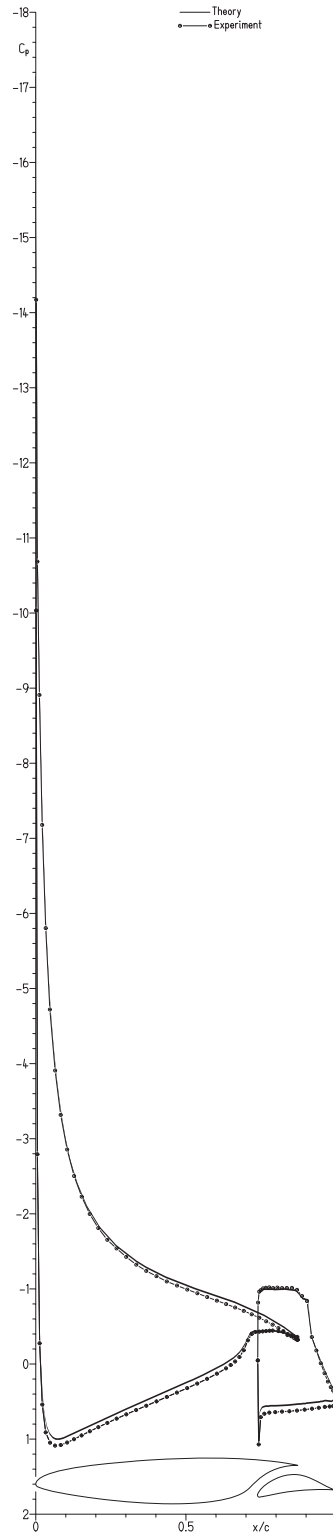
(d) $\alpha = 16.29°$.

Figure 10.- Concluded.
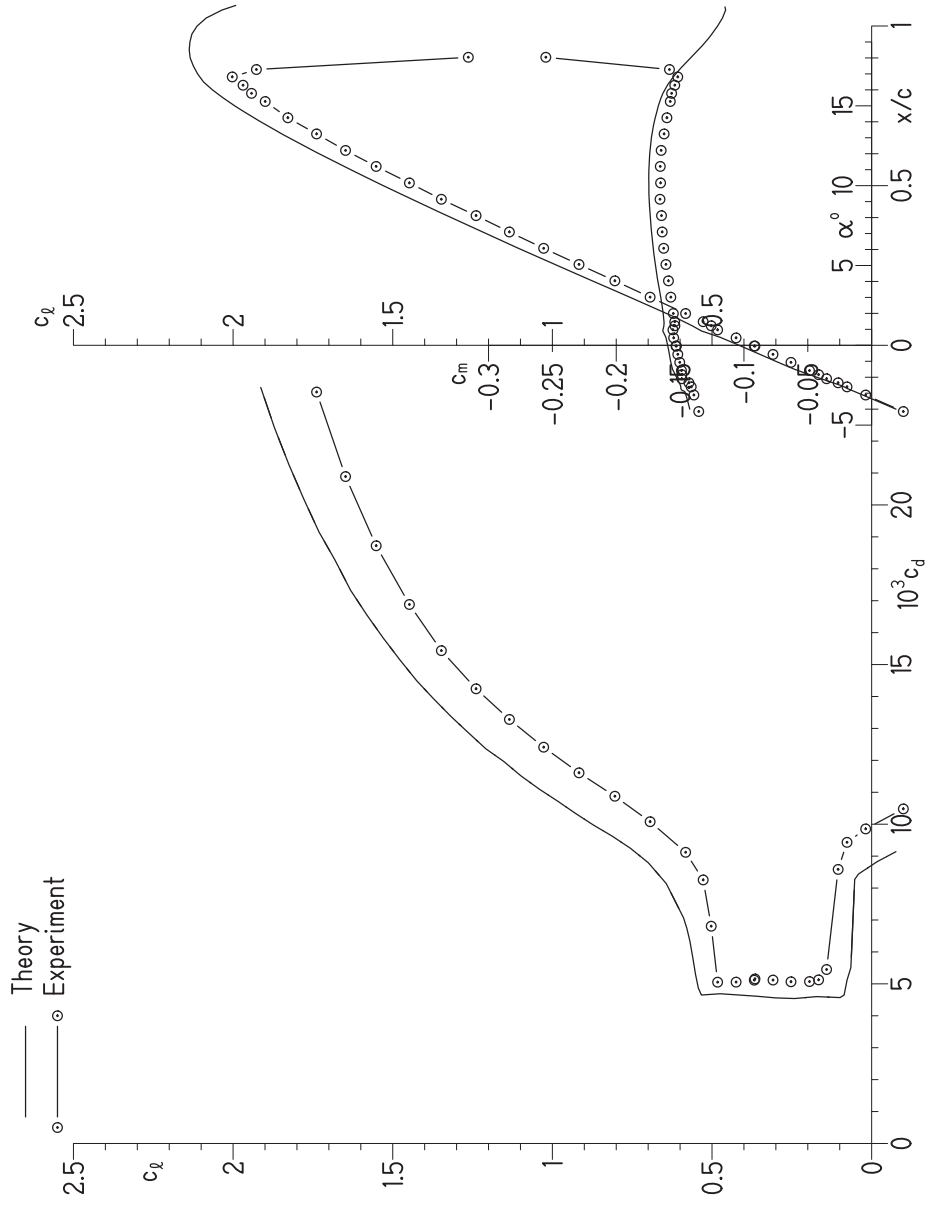
(a) $R = 3.0 \times 10^6$.

Figure 11.- Comparison of theoretical and experimental section characteristics at $M = 0.10$ with transition free.
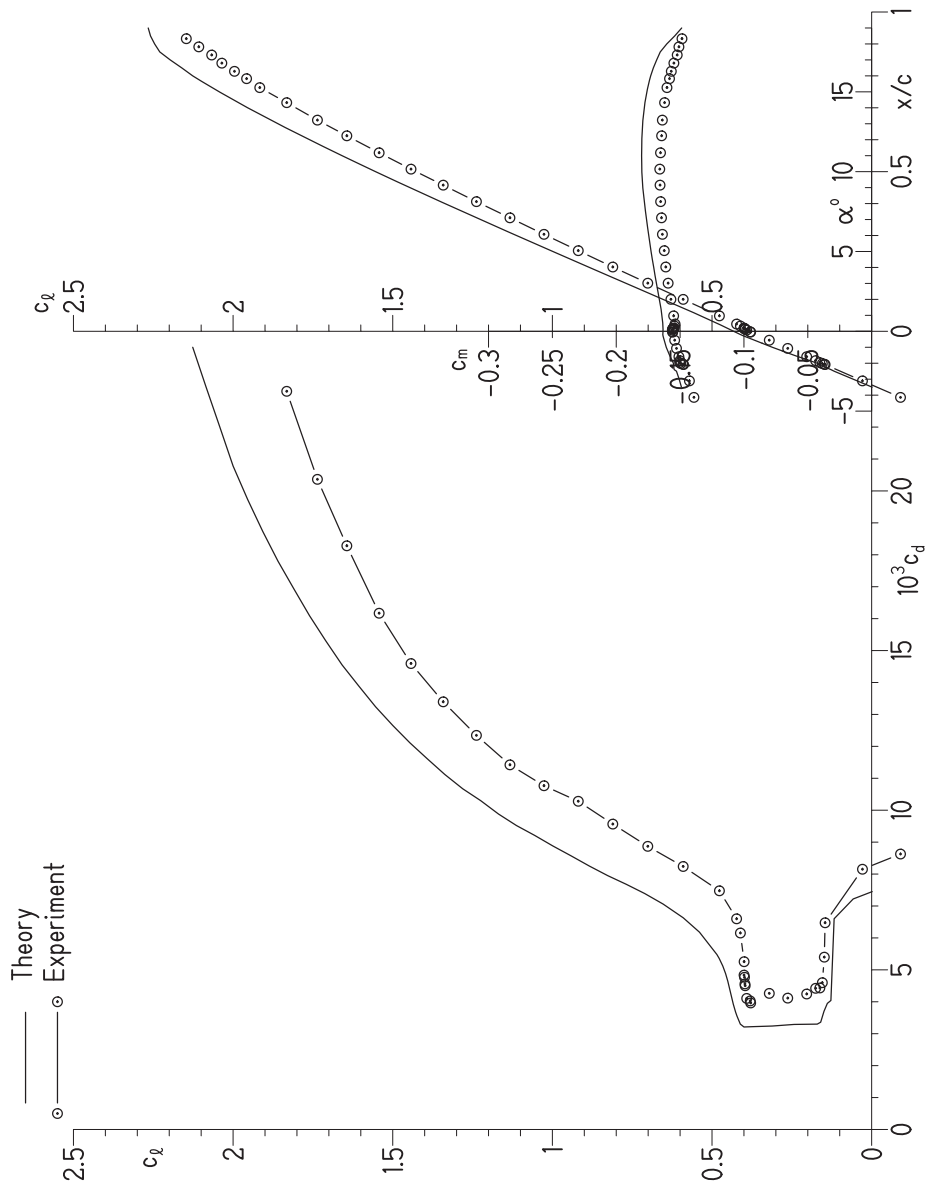
(b) R = 6.1 × 10⁶.

Figure 11.- Concluded.

(a) $R = 3 \times 10^6$ with transition free.
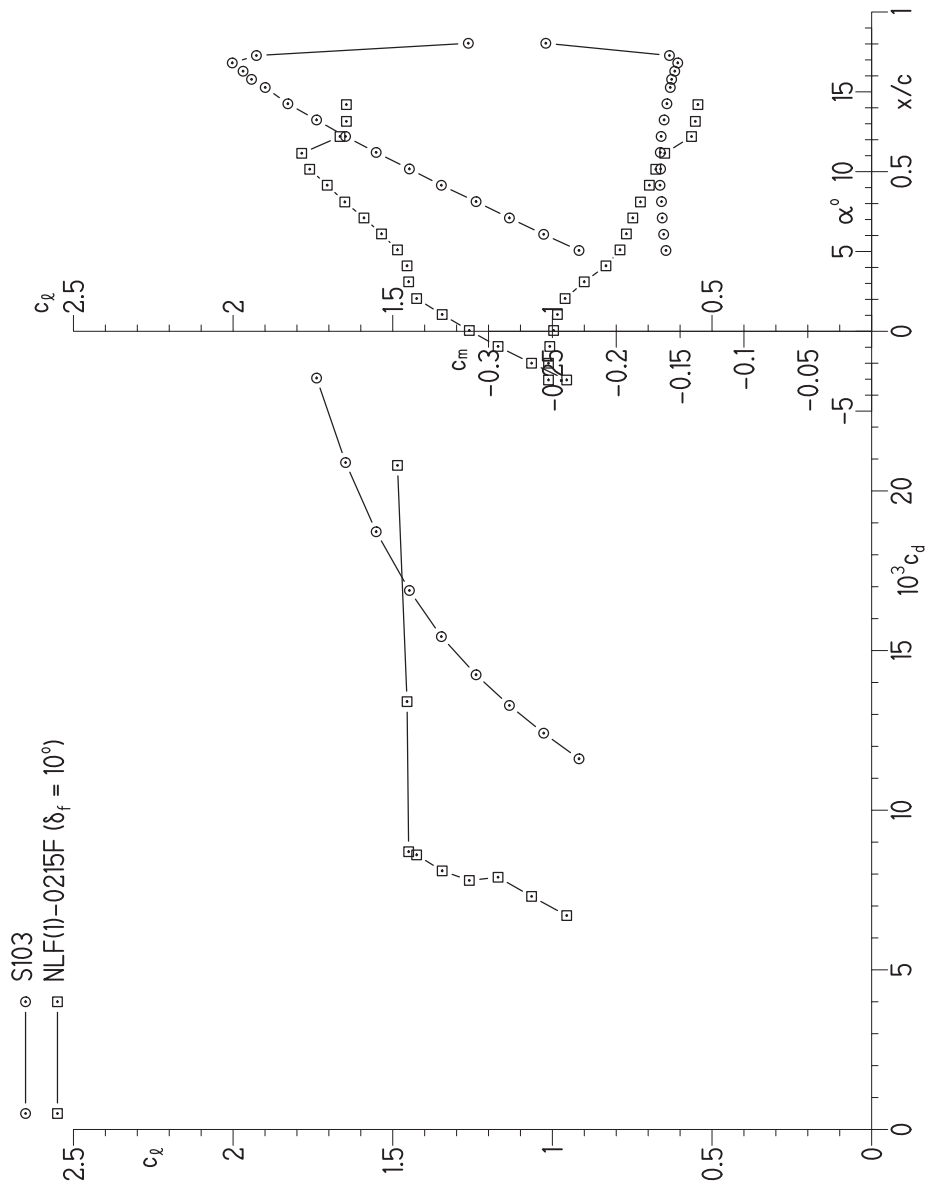
Figure 12.- Comparison of experimental section characteristics of S103 and NASA NLF(1)-0215F airfoils at $M = 0.1$ with transition free.
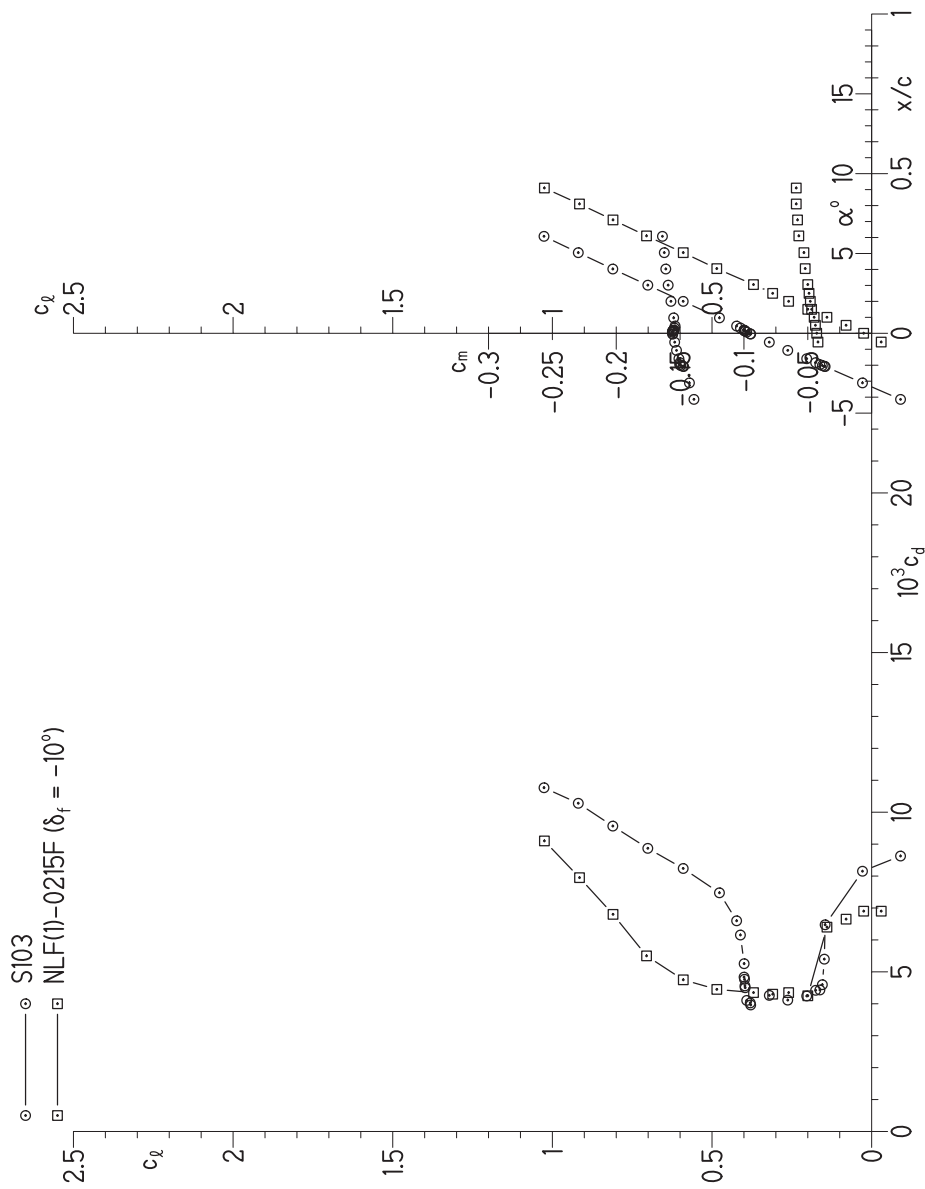
(b) $R = 6 \times 10^6$.

Figure 12.- Concluded.

1. REPORT DATE *(DD-MM-YYYY)*	2. REPORT TYPE	3. DATES COVERED *(From - To)*
01-04-2012	Contractor Report	08-15-2001 - 11-30-2004

4. TITLE AND SUBTITLE	5a. CONTRACT NUMBER
An Exploratory Investigation of a Slotted, Natural-Laminar-Flow Airfoil	NAS1-01076
	5b. GRANT NUMBER
	5c. PROGRAM ELEMENT NUMBER

6. AUTHOR(S)	5d. PROJECT NUMBER
Somers, Dan M.	5e. TASK NUMBER
	5f. WORK UNIT NUMBER
	561581.02.08.07.46.04

7. PERFORMING ORGANIZATION NAME(S) AND ADDRESS(ES)	8. PERFORMING ORGANIZATION REPORT NUMBER
NASA Langley Research Center Hampton, Virginia 23681-2199	

9. SPONSORING/MONITORING AGENCY NAME(S) AND ADDRESS(ES)	10. SPONSOR/MONITOR'S ACRONYM(S)
National Aeronautics and Space Administration Washington, DC 20546-0001	NASA
	11. SPONSOR/MONITOR'S REPORT NUMBER(S)
	NASA/CR-2012-217560

12. DISTRIBUTION/AVAILABILITY STATEMENT
Unclassified - Unlimited
Subject Category 02
Availability: NASA CASI (443) 757-5802

13. SUPPLEMENTARY NOTES

Langley Technical Monitor: James M. Luckring

14. ABSTRACT

A 15-percent-thick, slotted, natural-laminar-flow (SNLF) airfoil, the S103, for general aviation applications has been designed and analyzed theoretically and verified experimentally in the Langley Low-Turbulence Pressure Tunnel. The two primary objectives of high maximum lift and low profile drag have been achieved. The constraints on the pitching moment and the airfoil thickness have been satisfied. The airfoil exhibits a rapid stall, which does not meet the design goal. Comparisons of the theoretical and experimental results show good agreement. Comparison with the baseline, NASA NLF(1)-0215F airfoil confirms the achievement of the objectives.

15. SUBJECT TERMS

Aerodynamics; Airfoils; Laminar flow; Wind tunnel experiment

16. SECURITY CLASSIFICATION OF:			17. LIMITATION OF ABSTRACT	18. NUMBER OF PAGES	19a. NAME OF RESPONSIBLE PERSON
a. REPORT	b. ABSTRACT	c. THIS PAGE			STI Help Desk (email: help@sti.nasa.gov)
					19b. TELEPHONE NUMBER *(Include area code)*
U	U	U	UU	62	(443) 757-5802